Contrib Mineral Petrol (2007) 153:647–667
DOI 10.1007/s00410-006-0168-2

ORIGINAL PAPER

Laser Ablation ICPMS study of trace element partitioning between plagioclase and basaltic melts: an experimental approach

Mario Aigner-Torres · Jon Blundy · Peter Ulmer · Thomas Pettke

Received: 19 April 2006 / Accepted: 27 November 2006 / Published online: 17 January 2007

Abstract Plagioclase-melt partition coefficients (D) for 34 trace elements at natural concentration levels were determined experimentally in a natural MORB composition at atmospheric pressure using thin Pt-wire loops. Experiments were carried out at three temperatures (1,220, 1,200, and 1,180°C), and at three different oxygen fugacities (fO_2 = IW, QFM, air) in order to assess the effect of fO_2 on the partitioning of elements with multiple valence (Fe, Eu, Cr). Run products were analyzed by laser-ablation ICP-MS. Most trace element Ds increase slightly as temperature decreases, except for D_{Zr}, D_{Fe}, D_{Eu} and D_{Cr} that vary systematically with fO_2. Applying the Lattice Strain Model to our data suggests the presence of Fe^{2+} entirely in the octahedral site at highly to moderate reducing conditions, while Fe^{3+} was assigned wholly to the tetrahedral site of the plagioclase structure. Furthermore, we provide a new quantitative framework for understanding the partitioning behaviour of Eu, which occurs as both 2+ and 3+ cations, depending on $fO_2$and confirm the greater compatibility of Eu^{2+}, which has an ionic radius similar to Sr, relative to Eu^{3+} in plagioclase and the higher Eu^{2+}/Eu^{3+} under reducing conditions. For petrogenetic basaltic processes, a combined fractionation of Eu^{2+}–Sr and Fe–Mg by plagioclase has considerable potential as an oxybarometer for natural magmatic rocks.

Keywords Trace elements · Melting experiments · Plagioclase · LA-ICPMS

Communicated by T. L. Grove.

M. Aigner-Torres · P. Ulmer · T. Pettke
Institute of Mineralogy and Petrography,
Swiss Federal Institute of Technology,
ETH Zentrum NO, 8092 Zürich, Switzerland

J. Blundy
CETSEI, Department of Earth Sciences,
University of Bristol, Wills Memorial Building,
Bristol BS8 1 RJ, UK

M. Aigner-Torres (✉)
Department of Petroleum Engineering,
University of Campinas (DEP-FEM-UNICAMP),
6122 Campinas, 13083-970, Brazil
e-mail: mario@dep.fem.unicamp.br

Present Address:
T. Pettke
Institute of Geological Sciences, University of Bern,
Baltzerstrasse 1+3, 3012 Bern, Switzerland

Introduction

Mineral-melt trace element partition coefficients (D) are widely used in modeling of magmatic processes. In order to select the appropriate D for a particular magmatic problem it is essential to understand how Ds vary with intensive parameters, such as pressure, temperature and fO_2, as well as with composition. Plagioclase with its wide occurrence as a rock-forming mineral and its slow rate of intracrystalline diffusion (Grove et al. 1984a, b;Morse 1984) make it ideally suited to reconstructing the trace element content of the melts from which it grew, provided that appropriate trace element Ds are available. Of particular interest are Mg and Fe, which occur as minor or trace elements in plagioclase and therefore have the potential to reveal the evolution of Mg/Fe ratios in evolving magma. Similarly, Fe and Eu occur as both 2+ and 3+ ions in magmas and D_{Fe} and D_{Eu} can be used to constrain the

redox state of a magma. There are various natural and experimental studies in the literature where contents of certain trace elements in plagioclase have been routinely reported by microanalytical techniques (e.g., Phinney 1994; Peters et al. 1994; Wilke and Behrens 1999; Blundy 1997; Simon et al. 1994). There are, however, only few experiments have been carefully designed and analyzed for measurements of a large number of trace elements (e.g., Bindeman et al. 1998). In this study we report a series of experiments performed at high temperatures and varying fO_2 using a natural plagioclase-phyric basalt starting material. Laser ablation inductively coupled plasma mass spectrometer was used to analyze the run products for a large number of trace elements.

Experimental and analytical procedures

Starting material

A single starting material (ALV-3352-7) was used for all experiments. ALV-3352-7 is a natural, glassy and sparsely phyric pillow bud collected by the submersible Alvin from the Moai lava flow on the South East Pacific Rise at 18°110 (Sinton et al. 1999). It consists of a large amount of fresh glass, up to 10% phenocrysts of plagioclase, with minor olivine and traces of spinel. The freshest parts of sample ALV-3352-7 were reduced to powder by grinding aliquots of representative mechanical splits. Samples were then finely crushed in an agate mortar under acetone. Complete chemical analysis of ALV-3352-7, including trace elements, can be found in Table 1.

Experimental techniques

For each experiment approximately 50 mg of ALV-3352-7 powder was sintered onto a loop of 0.05 mm diameter platinum wire for no longer than 15 min. No pre-saturation of Pt with iron was employed, since the effective thickness of the Pt-wire minimized sample iron loss. The Pt-wire loop was suspended in the hot spot of a Gero 1 atm vertical gas-mixing furnace. Temperature was measured by a type S (Pt_{90}–Rh_{10}) thermocouple located just above the sample and a second, type B ($Pt_{94}Rh_6$–$Pt_{70}Rh_{30}$) thermocouple located in between the heating elements to control potential thermocouple poising in reducing atmosphere inside the furnace. The thermocouple was calibrated against the melting point of gold (1,064°C) and deviations are on the order of ±2°C. Oxygen fugacity was controlled by H_2/CO_2 gas mixture regulated by two Tylan mass flow controllers and calibrated in the hot spot of the furnace by determining the iron-wüstite and Ni-NiO equilibria at 1,200°C, with an error estimated at ±0.1 log unit. Gas flow rates were maintained constant at 0.5 cm^3/s for the 4.5 cm diameter furnace tube. This is sufficient to fix fO_2 while minimizing the extent of sodium loss from the charge. Since plagioclase is a difficult mineral to nucleate and grow experimentally, it took several trial and error experiments to optimize the technique to grow homogeneous crystals sufficiently large for LA-ICP-MS analysis (>40 μm diameter). The experimental charges were initially held slightly above their liquidus for a certain time (typically 2 h), allowing redox equilibration with the melt without completely destroying all plagioclase nuclei. They were subsequently cooled at a constant rate to the final run temperature, where they were left to equilibrate. Total run durations were up to about 1 week. Cooling rates varied from 1°C/min down to 1°C/h until reaching the final experimental temperature. Scatter around the values of some of the measured *D*s may be related to these cooling rate variations, and consequently to kinetic effects. Normally, our averaged partition coefficients (*D*s) within a certain run show less variation than *D*s averaged between charges with different cooling rates. Samples were drop-quenched into water by fusing the fine Pt suspension wire, and the quenched charges were mounted in an epoxy resin holder and polished sections made for petrographic and analytical analysis. Details of the experimental conditions, cooling history and resulting phase assemblage for representative runs are summarized in Table 2.

Iron and sodium loss

The extent of Fe and Na loss in experiments at one atmosphere in gas mixing furnaces is a long-standing problem in experimental petrology and some alternative approaches have been used including pre-saturation of the Pt-wire (see Borisov and Jones 1999; Tormey et al. 1987a, b; Grove 1981, and references therein). Because of the use of very thin Pt-loops with high average melt/loop mass ratio, Fe loss was comparable to the pre-saturation techniques, being up to 12% relative for experiments performed at the IW buffer at a moderate cooling rate. Fe loss is less at higher fO_2. Sodium loss on the other hand, still poses serious problems under the 1 atm experiments reaching in the present experiments nearly 40% in the worst case. Sodium loss is thought to depend on fO_2, temperature, run duration, size of sample material, gas flow rate and bulk chemical composition (see Tormey et al. 1987, b). Our very low fO_2 runs shown the strongest increase in vol-

Table 1 Composition of starting material and method comparisons

	Bulk rock[a]	Run no. 23[b]				Plagioclase[c]				Matrix glass[c]			
	XRF	EMPA[a]		LA-ICP-MS[a]		EMPA		LA-ICP-MS		EMPA		LA-ICPMS	
n[c]		6	σ	4	σ	50	σ	17	σ	20	σ	20	σ
SiO_2 (wt%)	50.4	49.5	0.4	50.8	0.17	48.0	1.4	48.9	6.1	50.2	0.1	51.2	4.2
TiO_2 (wt%)	1.31	1.24	0.06	1.07	0.005	0.039	0.014	0.028	0.007	1.33	0.05	1.15	0.03
Al_2O_3 (wt%)	15.53	15.98	0.08	16.99	0.05	32.5	0.9	32.67	3.3	15.2	0.1	15.7	1.2
FeO (wt%)	9.48	8.36	0.12	8.50	0.09	0.427	0.075	0.413	0.053	9.14	0.10	8.96	0.85
MnO (wt%)	0.16	0.172	0.025	0.162	0.001	0.012	0.004	0.005	0.001	0.177	0.046	0.173	0.009
MgO (wt%)	8.27	7.89	0.05	7.68	0.04	0.239	0.042	0.264	0.048	8.16	0.04	7.95	0.73
CaO (wt%)	12.55	12.33	0.13	12[d]	0.0	16.3	1.0	16.3[d]	0.0	12.4	0.1	12.4[d]	0.0
Na_2O (wt%)	2.55	2.39	0.09	2.6	0.01	1.99	0.51	2.17	0.87	2.47	0.05	2.68	0.40
K_2O (wt%)	0.08	0.08	0.01	0.083	0.001	0.012	0.008	0.011	0.004	0.077	0.021	0.084	0.004
P_2O_5(wt%)	0.11	0.16	0.06							0.097	0.012		
Total	100.4	98.1		100.20		99.5		100.8		99.1		100.3	
Li (ppm)				5.94	0.64			1.44	0.57			6.17	1.69
Be (ppm)				0.24	0.04			<2.10				4.20	3.47
Sc (ppm)				36.8	0.2			0.847	0.167			40.8	0.8
Cr (ppm)				301	6			12.51	4.05	342	118	357	15
Rb (ppm)				0.835	0.022			0.425	0.402			0.891	0.109
Sr (ppm)				98.9	0.9			156	11			98.6	1.1
Y (ppm)				22.54	0.19			0.177	0.037			25.4	0.7
Zr (ppm)				60.73	0.73			0.171	0.121			67.2	1.4
Nb (ppm)				1.58	0.07			0.198	0.162			1.54	0.09
Cs (ppm)				0.024	0.015			0.203	0.198			0.109	0.104
Ba (ppm)				6.00	0.08			1.37	0.40			6.53	0.26
La (ppm)				2.28	0.07			0.139	0.058			2.47	0.05
Ce (ppm)				7.13	0.05			0.441	0.289			7.80	0.17
Pr (ppm)				1.20	0.02			0.091	0.074			1.31	0.07
Nd (ppm)				7.05	0.22			0.226	0.092			7.71	0.34
Sm (ppm)				2.49	0.05			0.166	0.148			2.80	0.17
Eu (ppm)				0.99	0.03			0.230	0.059			1.11	0.07
Gd (ppm)				3.21	0.14			0.198	0.110			3.63	0.16
Tb (ppm)				0.598	.015			0.035	0.026			0.698	0.029
Dy (ppm)				4.06	0.17			0.101	0.066			4.58	0.22
Ho (ppm)				0.89	0.04			0.075	0.057			1.03	0.05
Er (ppm)				2.54	0.12			0.068	0.015			2.85	0.17
Tm (ppm)				0.361	0.004			0.033	0.027			0.409	0.035
Yb (ppm)				2.52	0.09			0.122	0.106			2.90	0.22
Lu (ppm)				0.360	0.008			0.033	0.019			0.417	0.029
Hf (ppm)				1.60	0.09			0.084	0.037			1.93	0.11
Ta (ppm)				0.720	0.026			0.066	0.057			0.103	0.020
Pb (ppm)				0.189	0.020			0.844	1.326			0.444	0.125
Th (ppm)				0.095	0.009			0.071	0.070			0.109	0.021
U (ppm)				0.050	0.014			0.221	0.157			0.058	0.021

[a] Whole rock XRF (SOEST, Hawai), EMPA (University of Vienna), LA-ICPMS (ETH Zurich), and SIMS (WHOI, Mass) measurements

[b] Fused whole rock, from Table 2

[c] n number of analysis; $\pm 1\sigma$ standard deviation of the mean

[d] CaO from EMPA used as internal standard

atilization of Na (Table 2). This is consistent with Phinney (1992), who reported up to 60% Na loss under similar experimental conditions. One possible side effect of this combined Fe and Na loss is to raise the liquidus temperature, enhancing the crystallization of plagioclase from 4 to 9 % with increasing run duration from 97 to 166 h associated with an increased Na- and Fe-loss from 10.6/1.2 to 14.5/5.6 wt%. This is evident from Runs 25 and 34 conducted at the same isotherm (1,180°C) with different cooling rates.

Electron microprobe analysis (EMP)

Major and minor elements were analyzed with a SX100 Cameca electron microprobe at the Institute of Petrology, University of Vienna. An accelerating po-

Table 2 Experimental conditions and run products

Run no.	Ramp (°C/h)	T (°C)	Duration (h)	log fO_2	Modes[a]					Na loss[b]	Fe loss[b]	X^{c}_{An}
					pl	sp	ol	cpx	gl			
23	1	1,260	5	–7.84	–	–	–	–	100	6.3	11.8	–
16	10	1,220	99	–11.68	1	–	–	–	99	33.6	11.0	0.763 ± 7
28	60	1,220	97	–8.18	tr	–	–	–	99	5.9	2.1	0.792 ± 3
29	60	1,220	97	–0.68	1	tr	–	–	99	6.3	2.6	0.755 ± 19
17	10	1,200	101	–11.93	3	–	–	tr	97	37.5	4.9	0.757 ± 7
31	60	1,200	97	–8.41	3	–	–	–	97	9.4	6.6	0.773 ± 32
33	60	1,200	97	–0.68	10	2	–	–	88	8.2	3.0	0.767 ± 6
35	60	1,180	97	–12.19	5	–	–	–	95	39.8	12.1	0.766 ± 11
25	1	1,180	166	–8.65	9	–	–	–	91	14.5	5.6	0.758 ± 5
34	60	1,180	97	–8.65	4	–	tr	–	96	10.6	1.2	0.735 ± 4
36	60	1,180	97	–0.68	15	3	–	–	82	3.1	0.2	0.734 ± 7

Thus, 0.763 ± 7 mean 0.763 ± 0.007

[a] Plagioclase *pl*, spinel *sp*, olivine *ol*, clinopyroxene *cpx*, glass *gl*, traces *tr*

Modes (vol %) are calculated by non-weighted least-square mass-balance

[b] Relative iron and sodium loss (in oxide %) estimated by non-weighted mass balance calculation

[c] Units after ± represent one standard deviation of least digit cited, on the base of replicate analyses

tential of 15 kV was used for all analyses. For glass analysis the beam current was 10 nA, defocused to 10 μm diameter. A 20 nA focused beam was used for mineral analyses. Counting times for all phases were 20s peak and 10s background, except for Na and K in glass (10s peak/5s background) and Fe, Mg, Ti and Mn in plagioclase—from 20 to 50s peak, in order to improve the counting statistics, which are 1–3% relative. Calibrations were performed using different natural and synthetic phases as standards for both minerals and glasses. A natural augite crystal was measured as a secondary standard and its 1σ standard deviations were, in wt%: 0.26 (SiO_2), 0.03 (TiO_2), 0.04 (Al_2O_3), 0.06 (FeO), 0.02 (MnO), 0.07 (MgO), 0.09 (CaO), and 0.05 (Na_2O). A labradorite from Lake County, Oregon, was analyzed periodically to check for consistency, and yielded relative precisions of ±5% for FeO and ±7% for MgO. Analysis of other standards were within 2σ of known values. Average error in total FeO (FeO_t) and MgO content of plagioclase due to analytical uncertainties are both about 0.02 wt% (1σ). These are in good agreement with errors averages related to compositional heterogeneity in run charges. PAP correction procedures were used to convert specimen/standard intensity ratios into concentrations.

Laser ablation ICP-MS (LA-ICPMS)

LA-ICPMS analyses were performed at the Institute of Isotope Geochemistry and Mineral Resources (ETH-Zürich) using a 193 nm ArF excimer laser system (Günther et al. 1997) combined with an ELAN 6100 quadrupole ICP-MS. The NIST SRM610 glass was used to calibrate analytical sensitivities. Internal standardization required for element concentration calculations employed major element concentrations as determined by EPMA. Operating conditions were very similar to those reported in Pettke et al. (2004). Embedded, polished capsules were loaded with the external standard in a 5 cm^3 ablation cell and put on the stage of a modified petrographic microscope operated in reflected light mode, allowing perfect positioning of the laser beam and selection of the appropriate spot size. Because transmitted light observation cannot be used for embedded capsules, any melt inclusions in the minerals cannot be optically identified. The acquisition of transient signals measured with 10 m dwell time per isotope; however, allows the identification of such melt inclusions in the analytical signal. Thus, the raw data were carefully screened for such inclusion signals and these were then manually removed. ICPMS operating conditions were daily optimized on SRM610 glass, ensuring low element-oxide production rates (Th/ThO tuned to >0.2%), robust plasma conditions and maximal signal-to-noise ratios for the isotopes of interest. Robust plasma conditions allow non-matrix matched calibration of LA-ICPMS signals (reviewed in Pettke 2006); hence, the SRM610 glass is perfectly suitable for calibration (see also Heinrich et al. 2003). Two standard deviation uncertainties on shot-to-shot reproducibilities are typically 2–5% on silicate phases unless signals are close to the respective detection limits (LOD), where counting statistics uncertainties may increase the overall uncertainty up to a few tens of percent. Data reduction was performed using the Lamtrace program, following principles outlined in Longerich

et al. (1996). Each shot was filtered using the individual, shot-specific LOD based on the three sigma criterion (Longerich et al. 1996). It is worth noting that the LOD increases for any given element with decreasing pit size. Given the often small grains in our reaction products, we thus rarely obtained significant element concentrations for some of the elements analyzed.

Results

Overview of run products and data

Plagioclase is the liquidus phase in all of the experiments, irrespective of fO_2. The experimental runs produced homogeneous, euhedral to subhedral plagioclase crystals up to several 100 μm in length (Fig. 1). The selected ten runs shown in Table 2 have high glass contents (>80%), giving large areas for analysis. All run products were very similar at the highest isotherm, but slight differences among phase appearance due to different oxygen fugacities and possibly cooling rates were observed. In addition to plagioclase and glass, a few traces of olivine and clinopyroxene appear. Spinel is a common phases at oxidizing conditions, being usually subhedral and showing sieve-texture within plagioclase crystals. Thus, at least for some runs, spinel could have appeared on the liquidus prior to the formation of plagioclase. The first oxide phase to crystallize is Fe-rich spinel with 65–68% Fe_2O_3, 5% FeO, 0.7% TiO_2, 17–18% MgO, and 7–9% Al_2O_3. Cr_2O_3 decreases with temperature from 0.65 to 0.04 wt%. The chemical variation in the other phases is not

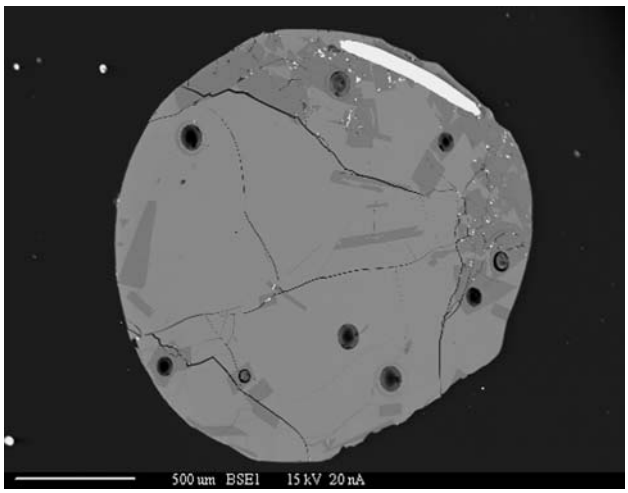

Fig. 1 Back-scattered electron image of run 25 showing analysis spots (laser ablation craters) in coexisting glass and plagioclase at quench temperature of 1,180°C and QFM buffer conditions. Photo shows the entire experimental charge cross section

further considered here. Major and trace element analysis of plagioclases and glasses are listed in Tables 3 and 4, respectively. All the plagioclases from this study are anorthite rich and exhibit a very narrow range in composition (73–79 mol%; Table 2). Major element homogeneity of different synthesized plagioclase crystals were checked by performing line profiles and, as in Phinney (1992), large crystals were used in order to avoid the possible effects of secondary fluorescence during EMP analyses. Calculated average relative standard deviations (RSD) on multiple analyses were better than 1% for SiO_2 and Al_2O_3, 1.5% for CaO, and 5% for Na_2O. For FeO and MgO variations are better than 20 and 10%, respectively. The minor elements TiO_2, MnO and K_2O have very large variations due to their low content and poor accuracy by EMP.

Trace element concentrations in plagioclases have average RSDs on multiple analyses that vary depending on the element in question. For Sr, maximum averages are close to 10%, but for Cr and other highly incompatible elements (e.g., heavy rare earth elements, HREE), the associated RSD average can be much higher, since these elements are essentially at the limits of detection of the LA-ICP-MS. Calculated average RSDs from multiple analyses for both major and trace elements in glass run products are typically much more homogeneous when compared with plagioclases (Tables 3, 4). This can be attributed to the higher concentrations of most of the elements measured in glasses and due to the larger laser pit sizes (80 μm), allowing better constrained measurements and LOD.

Homogeneity of the newly grown plagioclase crystals alone does not guarantee that near equilibrium conditions were attained during the experiments. The lack of zoning is a further indication that at least steady state conditions were achieved during the run time. Classical reversal experiments could not be performed because it resulted to be impossible to grow homogenous and large enough crystals for EMP and LA-ICP-MS analysis by forward melting experiments. Only by slow cooling from just above the liquidus where only a minimum of nuclei survived resulted such crystals. As a additional test for the attainment of equilibrium we present a comparison of the $CaO/(Na_2O + K_2O)$ partitioning between homogenous, euhedral plagioclase and quenched liquid (glass) from this study and literature data obtained for basaltic systems at one bar (Bender et al. 1978; Grove and Bryan 1983; Tormey et al. 1987, b; Grove et al. 1990; Bartels et al. 1991, 1994; Yang et al. 1996; Thy et al. 1999; Sano et al. 2001). The diagram (Fig. 2) reveals two important observations: (i) the data points from our experiments

Table 3 Electron microprobe (wt%) analyses of run products

Temp (°C)	Run no.	log fO_2	Phase	n[a]	SiO_2	σ	TiO_2	σ	Al_2O_3	σ	FeO	σ	MnO	σ	MgO	σ	CaO[b]	σ	Na_2O	σ	K_2O	σ	P_2O_5	σ	Total
1,220	16	–11.7	pl	5	49.98	0.31	0.05	0.03	31.62	0.16	0.30	0.02	0.03	0.02	0.28	0.01	15.26	0.24	2.61	0.07	0.02	0.01	0.04	0.01	100.15
			gl	7	50.77	0.07	1.31	0.05	15.04	0.08	8.40	0.10	0.16	0.02	8.74	0.11	12.27	0.09	1.65	0.06	0.07	0.00	0.10	0.12	98.50
	28	–8.18	pl	2	48.09	0.10	0.05	0.01	31.34	0.22	1.07	0.24	0.02	0.01	0.23	0.04	15.92	0.28	2.31	0.06	0.01	NA	NA	NA	99.02
			gl	5	49.80	0.19	1.23	0.06	16.13	0.08	8.64	0.09	0.18	0.03	7.54	0.57	12.33	0.09	2.34	0.03	0.08	0.02	0.08	0.04	98.43
	29	–0.68	pl	3	49.63	1.18	0.07	0.01	29.03	0.53	2.70	0.13	0.03	0.02	*0.13*	0.03	15.02	0.39	2.68	0.22	0.02	0.01	NA	NA	99.26
			gl	5	50.41	0.25	1.40	0.04	14.20	0.08	8.82	0.05	0.22	0.02	9.58	0.37	12.06	0.16	2.31	0.07	0.09	0.03	0.11	0.01	99.21
1,200	17	–11.9	pl	8	50.06	0.36	0.05	0.03	31.35	0.26	0.32	0.04	0.01	0.01	0.31	0.02	15.16	0.22	2.67	0.07	0.03	0.01	0.09	0.05	100.00
			gl	12	51.35	0.14	1.50	0.05	13.86	0.10	8.90	0.13	0.21	0.03	8.88	0.05	12.29	0.12	1.44	0.05	0.07	0.01	0.11	0.08	98.55
	31	–8.41	pl	6	49.42	0.48	0.06	0.01	30.80	0.20	1.19	0.06	0.01	0.00	0.36	0.11	15.37	0.20	2.48	0.43	0.03	0.01	NA	NA	99.72
			gl	5	49.97	0.31	1.32	0.05	15.26	0.09	9.04	0.07	0.19	0.03	9.48	0.35	12.10	0.13	2.30	0.08	0.08	0.01	0.09	0.02	99.90
	33	–0.68	pl	2	48.84	0.46	0.07	0.01	29.75	0.16	2.41	0.02	0.02	0.00	0.47	0.03	15.35	0.21	2.55	0.07	0.03	0.01	NA	NA	99.47
			gl	4	49.76	0.14	1.32	0.07	15.40	0.13	8.90	0.12	0.18	0.01	8.69	0.51	12.13	0.10	2.37	0.02	0.10	0.02	0.11	0.03	98.97
1,180	35	–12.2	pl	5	49.21	0.43	0.06	0.01	30.90	0.35	0.31	0.03	0.02	0.01	0.29	0.08	15.30	0.28	2.56	0.11	0.03	0.01	NA	NA	98.67
			gl	5	51.78	0.33	1.41	0.05	14.82	0.17	8.71	0.12	0.20	0.03	9.31	0.71	12.30	0.13	1.49	0.05	0.08	0.02	0.02	0.00	100.16
	25	–8.65	pl	3	48.70	0.19	0.06	0.01	30.78	0.32	0.80	0.03	0.03	0.01	0.33	0.02	15.19	0.15	2.66	0.07	0.02	0.01	NA	NA	98.56
			gl	5	50.64	0.49	1.47	0.07	14.14	0.09	9.72	0.12	0.20	0.03	9.73	0.74	12.08	0.11	2.14	0.05	0.09	0.02	0.11	0.04	100.35
	34	–8.65	pl	5	49.30	0.48	0.04	0.01	30.10	0.24	0.86	0.08	0.01	0.00	0.38	0.06	14.80	0.16	2.93	0.04	0.02	0.01	NA	NA	98.42
			gl	4	49.81	0.26	1.42	0.07	14.51	0.16	9.63	0.11	0.19	0.02	8.68	0.56	12.18	0.18	2.21	0.10	0.08	0.02	0.10	0.04	98.87
	36	–0.68	pl	6	48.96	0.60	0.07	0.01	28.42	0.24	2.64	0.18	0.03	0.01	0.45	0.12	14.55	0.15	2.89	0.07	0.02	0.01	NA	NA	98.01
			gl	5	51.93	0.23	1.71	0.09	13.54	0.08	8.42	0.09	0.22	0.03	9.34	0.50	11.28	0.15	2.49	0.11	0.10	0.02	0.14	0.04	99.19

[a] n number of analyses; ± 1σ standard deviation (SD) of the mean

[b] Average EMP value, used as Internal Standard for the quantification of LA-ICPMS signals

NA Not available

Table 4 Laser Ablation ICP-MS (ppm) analyses of selected run products

Temp (° C)	Run no.	log O_2	Phase	n^a	Li	σ	Mg	σ	K	σ	Sc	σ	Ti	σ
1,220	16	–11.7	pl	3	1.67		1,942	124	128	16	0.67	0.09	278	15
			gl	4	4.55	0.12	50,232	770	584	8	41.23	0.51	7,047	57
	28	–8.18	pl	2	14.71	NA	2,395	418	110	1	<2.93	NA	309	94
			gl	3	4.58	0.51	4,8031	277	637	1	38.11	0.45	6,535	31
	29	–0.68	pl	2	<5.20	NA	1,840	256	111	7	1.38	0.11	234	54
			gl	5	6.37	0.73	49,565	532	659	5	39.73	0.65	6,827	37
1,200	17	–11.9	pl	3	<2.13	NA	1,250	77	62	9	0.72	NA	113	10
			gl	3	5.76	0.78	5,1601	2,263	631	35	47.09	0.72	8,150	177
	31	–8.41	pl	5	1.65	0.69	1,873	229	136	12	0.65	0.21	266	23
			gl	3	5.62	0.68	49,433	345	670	8	40.14	0.30	7,015	73
	33	–0.68	pl	4	<18.44	NA	2,695	469	147	12	<2.94	NA	393	78
			gl	3	8.99	0.12	5,4048	258	715	2	43.79	0.27	7,549	41
1,180	35	–12.2	pl	4	<4.42	NA	2,495	269	161	25	<0.73	NA	284	55
			gl	3	3.88	0.30	51,689	851	612	1	42.78	0.66	7,394	26
	25	–8.65	pl	6	<2.09	NA	2591	569	163	36	1.06	0.12	362	77
			gl	3	6.82	0.67	49,513	1,523	690	26	43.48	1.95	7,664	322
	34	–8.65	pl	6	3.25	0.93	2,058	97	161	25	0.86	0.09	295	15
			gl	3	5.65	0.79	50,487	1,734	689	15	41.21	1.18	7181	122
	36	–0.68	pl	6	5.74	NA	2,781	173	215	26	4.97	1.58	1,043	435
			gl	3	8.46	0.30	52126	1,157	878	62	43.60	0.24	8,510	652

Temp (° C)	Run no.	log O_2	Phase	n^a	Cr	σ	Mn	σ	Fe	σ	Rb	σ	Sr	σ
1,220	16	–11.7	pl	3	13.16	NA	38	3	1,498	141	<0.06	NA	163.4	0.7
			gl	4	348.59	12.19	1,400	29	64290	1,147	0.64	0.09	95.3	0.3
	28	–8.18	pl	2	<53.79	NA	55	11	9,561	1,123	<0.48	NA	153.8	3.7
			gl	3	179.97	4.79	1,275	8	65,414	191	0.71	0.04	98.3	0.4
	29	–0.68	pl	2	<14.69	NA	44	4	15,914	2,087	<0.12	NA	135.1	5.8
			gl	5	53.63	13.30	1,311	13	67,065	1,002	0.84	0.01	95.2	0.5
1,200	17	–11.9	pl	3	12.34	NA	31	2	2,135	272	<0.06	NA	137.3	4.9
			gl	3	332.10	47.85	1577	33	66,563	2,033	0.62	0.10	95.9	2.6
	31	–8.41	pl	5	10.56	NA	39	6	7,601	298	0.10	NA	154.2	2.7
			gl	3	235.38	0.32	1,329	16	66,375	468	0.88	0.07	94.7	0.3
	33	–0.68	pl	4	<46.19	NA	57	13	22,537	1,018	<0.34	NA	150.4	5.5
			gl	3	14.80	1.91	1410	12	66,457	417	0.86	0.03	93.0	0.4
1,180	35	–12.2	pl	4	<9.90	NA	49	8	1,639	179	<0.10	NA	163.7	6.3
			gl	3	334.17	1.07	1,433	14	66,035	855	0.65	0.01	94.2	0.3
	25	–8.65	pl	6	5.85	NA	77	20	8,838	1,005	0.89	NA	150.4	3.6
			gl	3	16.04	0.72	1,429	55	71,972	1,906	0.73	0.06	91.7	1.6
	34	–8.65	pl	6	4.31	0.84	36	1	6211	471	0.05	0.00	158.3	4.3
			gl	3	223.50	10.17	1,410	35	72,129	1,497	0.80	0.01	92.4	0.6
	36	–0.68	pl	6	160.21	49.48	278	99	41,033	4,059	0.18	N	150.1	10.0
			gl	3	10.21	2.38	1,514	39	61,683	1,510	1.46	0.19	95.8	2.7

Temp (°C)	Run no.	log O_2	Phase	n^a	Y	σ	Zr	σ	Nb	σ	Cs	σ	Ba	σ
1,220	16	–11.7	pl	3	0.21	0.03	0.21	0.06	<0.05	NA	<0.02	NA	1.88	0.29
			gl	4	25.81	0.06	69.02	0.46	1.75	0.03	0.03	NA	6.24	0.05
	28	–8.18	pl	2	<0.28	NA	1.37	NA	<0.54	NA	<0.11	NA	1.31	NA
			gl	3	23.60	0.07	63.19	0.65	1.61	0.04	0.02	0.00	5.81	0.03
	29	–0.68	pl	2	0.20	NA	2.15	NA	0.19	NA	0.09	NA	1.31	0.17
			gl	5	25.08	0.14	66.66	0.47	1.70	0.06	0.02	0.00	6.15	0.11
1,200	17	–11.9	pl	3	0.20	0.00	0.08	NA	<0.05	NA	<0.02	NA	0.96	0.33
			gl	3	30.26	1.04	79.30	1.82	2.01	0.11	0.03	NA	7.39	0.29
	31	–8.41	pl	5	0.19	0.07	0.10	NA	0.17	NA	0.34	0.03	1.53	0.30
			gl	3	25.62	0.15	68.06	0.29	1.70	0.04	0.58	NA	6.18	0.08
	33	–0.68	pl	4	0.73	0.11	1.28	NA	<0.48	NA	<0.12	NA	2.42	0.04
			gl	3	27.36	0.10	72.86	0.74	1.92	0.00	0.02	0.01	6.74	0.05

Table 4 continued

Temp (° C)	Run no.	log O_2	Phase	n^a	Li	σ	Mg	σ	K	σ	Sc	σ	Ti	σ
1,180	35	–12.2	pl	4	0.20	0.02	0.29	NA	<0.09	NA	<0.03	NA	2.31	0.46
			gl	3	26.87	0.20	72.07	0.69	1.77	0.01	0.01	0.00	6.80	0.15
	25	–8.65	pl	6	0.22	0.02	0.22	0.06	0.07	NA	<0.01	NA	1.62	0.25
			gl	3	27.31	1.03	73.18	2.90	1.83	0.09	0.01	0.00	6.62	0.25
	34	–8.65	pl	6	0.16	0.01	0.05	0.01	<0.03	NA	<0.01	NA	2.05	0.36
			gl	3	25.35	0.36	66.83	0.99	1.74	0.03	0.01	0.00	6.26	0.18
	36	–0.68	pl	6	0.29	0.05	0.77	NA	0.31	NA	<0.03	NA	2.14	0.37
			gl	3	31.03	2.13	86.67	9.69	2.24	0.29	0.03	0.01	7.73	0.68

Temp (° C)	Run no.	log O_2	Phase	n^a	Hf	σ	Ta	σ	Pb	σ	Th	σ	U	σ
1,220	16	–11.7	pl	3	<0.05	NA	0.03	NA	0.06	NA	<0.02	NA	<0.02	NA
			gl	4	1.90	0.08	0.83	0.01	0.02	0.00	0.12	0.01	0.05	0.01
	28	–8.18	pl	2	<0.58	NA	<0.16	NA	<0.54	NA	<0.11	NA	<0.15	NA
			gl	3	1.77	0.05	0.73	0.03	0.04	NA	0.11	0.01	0.08	0.00
	29	–0.68	pl	2	<0.17	NA	<0.05	NA	0.73	0.15	<0.04	NA	<0.03	NA
			gl	5	1.89	0.04	0.78	0.03	0.74	0.01	0.12	0.01	0.16	0.02
1,200	17	–11.9	pl	3	<0.06	NA	<0.02	NA	0.07	NA	<0.02	NA	<0.01	NA
			gl	3	2.23	0.04	0.94	0.02	0.05	0.03	0.13	0.00	0.06	0.03
	31	–8.41	pl	5	0.06	NA	0.06	0.02	0.08	NA	0.04	0.01	<0.01	NA
			gl	3	1.89	0.09	0.81	0.03	0.05	NA	0.12	0.01	0.08	0.02
	33	–0.68	pl	4	<0.53	NA	<0.15	NA	<0.43	NA	<0.10	NA	0.22	NA
			gl	3	2.05	0.01	0.86	0.01	0.18	0.02	0.12	0.01	0.43	0.01
1,180	35	–12.2	pl	4	<0.12	NA	<0.03	NA	<0.16	NA	<0.03	NA	<0.03	NA
			gl	3	2.09	0.05	0.85	0.02	0.03	0.00	0.11	0.01	0.05	0.00
	25	–8.65	pl	6	0.07	NA	0.03	0.01	0.12	NA	<0.01	NA	<0.01	NA
			gl	3	2.07	0.13	0.90	0.06	0.22	NA	0.12	0.01	0.20	0.03
	34	–8.65	pl	6	<0.03	NA	<0.01	NA	0.06	0.02	<0.01	NA	<0.01	NA
			gl	3	1.91	0.07	0.82	0.03	0.02	0.00	0.11	0.01	0.05	0.01
	36	–0.68	pl	6	0.37	0.11	0.18	NA	0.25	0.02	0.06	0.04	0.03	NA
			gl	3	2.39	0.30	1.06	0.11	0.09	0.01	0.15	0.03	0.28	0.03

Temp (° C)	Run no.	log O_2	Phase	n^a	La	σ	Ce	σ	Pr	σ	Nd	σ	Sm	σ
1,220	16	–11.7	pl	3	0.16	0.01	0.37	0.05	0.06	0.01	0.30	0.04	<0.12	NA
			gl	4	2.55	0.03	7.48	0.11	1.30	0.03	7.53	0.10	2.73	0.06
	28	–8.18	pl	2	0.20	NA	0.30	NA	<0.16	NA	<1.02	NA	<1.11	NA
			gl	3	2.31	0.07	6.86	0.07	1.20	0.02	7.08	0.14	2.59	0.04
	29	–0.68	pl	2	0.12	0.03	0.27	0.05	0.07	NA	0.29	NA	0.32	0.03
			gl	5	2.43	0.01	7.20	0.04	1.38	0.28	7.24	0.12	2.82	0.03
1,200	17	–11.9	pl	3	0.08	NA	0.27	0.07	0.04	0.01	0.22	0.02	<0.08	NA
			gl	3	3.02	0.13	8.77	0.32	1.49	0.05	8.92	0.30	3.22	0.14
	31	–8.41	pl	5	0.20	0.05	0.40	0.11	0.05	0.01	0.40	0.12	0.22	NA
			gl	3	2.62	0.07	7.42	0.12	1.28	0.01	7.38	0.20	2.71	0.10
	33	–0.68	pl	4	0.22	NA	0.33	0.02	0.26	NA	0.93	0.06	<0.85	NA
			gl	3	2.73	0.05	8.13	0.03	1.33	0.12	8.25	0.20	2.88	0.06
1,180	35	–12.2	pl	4	0.15	0.02	0.39	0.08	0.08	0.02	0.31	NA	<0.22	NA
			gl	3	2.55	0.05	7.68	0.04	1.32	0.02	7.87	0.10	2.93	0.04
	25	–8.65	pl	6	0.16	0.02	0.49	0.12	0.08	0.02	0.03	0.25	0.10	NA
			gl	3	2.74	0.10	8.10	0.32	1.38	0.03	8.14	0.35	2.96	0.11
	34	–8.65	pl	6	0.16	0.02	0.34	0.03	0.04	0.01	0.25	0.04	0.10	NA
			gl	3	2.57	0.05	7.56	0.12	1.30	0.02	7.53	0.13	2.74	0.06
	36	–0.68	pl	6	0.22	0.06	0.42	0.07	0.21	0.08	0.97	NA	<0.22	NA
			gl	3	3.10	0.31	9.37	0.65	1.59	0.15	9.41	0.85	3.39	0.22

Temp (° C)	Run no.	log O_2	Phase	n^a	Eu	σ	Gd	σ	Tb	σ	Dy	σ	Ho	σ
1,220	16	–11.7	pl	3	0.09	0.90	<0.11	NA	<0.02	NA	<0.08	NA	<0.02	NA
			gl	4	1.04	0.01	3.68	0.10	0.70	0.03	4.68	0.08	1.02	0.02
	28	–8.18	pl	2	0.24	NA	<1.18	NA	<0.17	NA	<0.59	NA	<0.12	NA
			gl	3	0.99	0.01	3.39	0.04	0.63	0.00	4.30	0.05	0.92	0.02
	29	–0.68	pl	2	0.13	NA	<0.32	NA	<0.04	NA	0.51	NA	0.08	NA
			gl	5	1.09	0.02	3.58	0.03	0.66	0.02	4.43	0.03	0.98	0.03

Table 4 continued

Temp (° C)	Run no.	log O_2	Phase	n^a	Li	σ	Mg	σ	K	σ	Sc	σ	Ti	σ
1,200	17	–11.9	pl	3	0.29	0.04	<0.13	NA	<0.01	NA	0.13	NA	<0.02	NA
			gl	3	1.10	0.07	4.24	0.18	0.83	0.06	5.48	0.20	1.17	0.04
	31	–8.41	pl	5	0.12	0.04	0.16	0.05	0.02	0.01	0.22	0.07	0.05	0.01
			gl	3	1.08	0.03	3.70	0.09	0.69	0.02	4.63	0.15	1.02	0.01
	33	–0.68	pl	4	<0.25	NA	<0.86	NA	0.17	NA	<0.45	NA	<0.11	NA
			gl	3	1.19	0.02	3.96	0.10	0.74	0.01	5.03	0.04	1.09	0.03
1,180	35	–12.2	pl	4	0.97	0.11	<0.19	NA	<0.04	NA	<0.12	NA	<0.02	NA
			gl	3	1.00	0.02	3.83	0.06	0.73	0.01	4.89	0.03	1.05	0.02
	25	–8.65	pl	6	0.11	0.03	0.28	NA	0.03	0.00	0.08	NA	0.04	0.00
			gl	3	1.15	0.07	3.88	0.18	0.73	0.03	4.93	0.16	1.09	0.03
	34	–8.65	pl	6	0.12	0.01	0.08	0.01	0.01	0.00	0.06	0.01	0.02	0.01
			gl	3	1.09	0.03	3.67	0.16	0.70	0.02	4.60	0.09	1.02	0.01
	36	–0.68	pl	6	0.20	NA	0.66	0.04	0.08	NA	0.72	NA	0.13	NA
			gl	3	1.30	0.08	4.33	0.32	0.82	0.05	5.62	0.35	1.22	0.06

Temp (° C)	Run no.	log O_2	Phase	n^a	Er	σ	Tm	σ	Yb	σ	Lu	σ
1,220	16	–11.7	pl	3	<0.07	NA	<0.02	NA	<0.09	NA	<0.01	NA
			gl	4	2.87	0.05	0.41	0.01	2.96	0.12	0.42	0.00
	28	–8.18	pl	2	<0.90	NA	<0.14	NA	<0.88	NA	<0.12	NA
			gl	3	2.51	0.05	0.37	0.02	2.68	0.04	0.39	0.02
	29	–0.68	pl	2	<0.24	NA	<0.04	NA	0.27	NA	<0.04	NA
			gl	5	2.74	0.02	0.41	0.01	2.86	0.05	0.40	0.02
1,200	17	–11.9	pl	3	<0.10	NA	<0.01	NA	<0.10	NA	<0.02	NA
			gl	3	3.28	0.15	0.49	0.02	3.51	0.17	0.48	0.00
	31	–8.41	pl	5	0.16	0.03	0.02	NA	<0.07	NA	<0.01	NA
			gl	3	2.85	0.11	0.40	0.01	2.85	0.09	0.41	0.02
	33	–0.68	pl	4	<0.60	NA	<0.11	NA	<0.71	NA	<0.12	NA
			gl	3	3.07	0.05	0.42	0.02	3.10	0.15	0.44	0.01
1,180	35	–12.2	pl	4	<0.14	NA	<0.04	NA	<0.25	NA	0.02	NA
			gl	3	2.97	0.07	0.43	0.01	3.06	0.10	0.44	0.02
	25	–8.65	pl	6	0.10	NA	0.01	NA	0.11	NA	<0.01	NA
			gl	3	2.94	0.16	0.43	0.04	3.10	0.07	0.44	0.02
	34	–8.65	pl	6	<0.04	NA	<0.01	NA	<0.05	NA	<0.01	NA
			gl	3	2.76	0.03	0.41	0.02	2.88	0.08	0.41	0.00
	36	–0.68	pl	6	0.48	NA	0.06	NA	0.50	NA	0.09	NA
			gl	3	3.49	0.25	0.50	0.04	3.55	0.21	0.50	0.05

[a] n number of analyses; ± 1σ standard deviation (SD) of the mean

NA Not available; values below direction limit show as in, e.g., <1.67

plot within range defined by the large number of comparable experiments from literature, except (ii) the three runs at low fO_2 and long run duration (#16, 17, and 35, open circles) that suffered 33–40% relative Na_2O-loss. These data point plot towards high CaO/(Na_2O + K_2O) values for the liquid phase because their sodium values are low. This behavior indicates that plagioclase grew rather early in the experiments and did not adjust their composition upon loss of sodium during the late stage of the experiments. The arrows indicate the shift of these samples when the Na-loss in the coexisting liquids are adjusted using the results from the least squares regression; after correction all three data point perfectly plot within the range defined by our other samples and the range covered by the literature data. This is consistent with very slow coupled CaAl–NaSi diffusion in plagioclase that does no exceed 10^{-18} cm^2/s for plagioclase of An_{80} at 1,200°C (e.g., Grove et al. 1984a, b; Morse 1984). Therefore, re-equilibration of early grown crystals is inhibited, except for the outermost rim that could not be quantitatively analyzed. In conclusion, all but the three experiments at low fO_2 show Ca–Na–K partitioning consistent with a large number of one bar experiments from literature; the three samples that suffered large sodium loss did not re-equilibrate with the changing liquid composition (for sodium–calcium) but records the equilibrium partitioning acquired in the early stages of the experiments when the crystals grew. Taking this shortcoming into consideration we have used all reported data for subsequent discussion of the trace and minor element partitioning behavior.

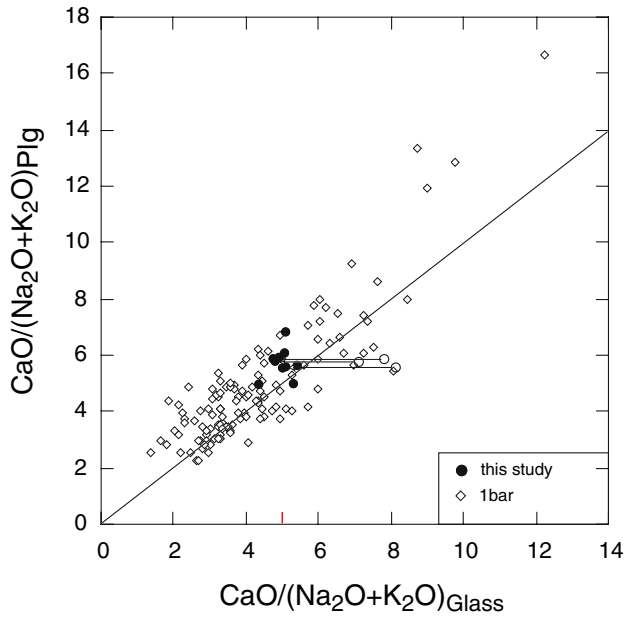

Fig. 2 $CaO/(Na_2O+K_2O)$—ratios (wt%) of plagioclase versus coexisting liquids (quenched glasses) from this study (*open* and *solid circles*) compared with 1 bar experimental data from the literature (*open diamonds*) taken from Bender et al. (1978); Grove and Bryan (1983); Tormey et al. (1987, b); Grove et al. (1990); Bartels et al. (1991); Baker et al. (1994); Yang et al. (1996); Thy et al. (1999); Sano et al. (2001). *Open circles* with *arrows* pointing to *solid circle* data points indicate run that have suffered >5 wt% Na_2O-loss; *arrow* indicate the shift of the data points when the liquid (glass) analyses are corrected for Na_2O-loss occurring in long run duration experiments at low fO_2 conditions (run# 16, 17, and 35). The *solid line* indicates the 1:1 partitioning of $CaO/(Na_2O + K_2O)$ between plagioclase and liquid and is only given for reference

Partition coefficients

*D*s for each experimental run, calculated from LA-ICP-MS analysis (Table 4) are summarized in Table 5. Figure 3 shows *D*values for different groups of elements according to their experimental temperatures and fO_2. We also compared the experimental Ds with those derived from plagioclase and glass analysis of the natural sample ALV-3352-7 analyzed by the same LA-ICP-MS technique (Table 1).

Majors elements (Si, Al, Ca, Na)

The concentrations of CaO, Al_2O_3, SiO_2, and Na_2O, which represent the main solid solution components in plagioclase, give very stable *D* values—calculated from microprobe analyses in Table 3. Averages for compatible and near-compatible elements, D_{Si} 0.97 ± 0.02, D_{Al} 2.07 ± 0.10, and D_{Ca} 1.26 ± 0.03, are independent of temperature and oxygen fugacity. Only D_{Na} shows a larger variation 1.34 ± 0.30—due to the likely coupled effect of fO_2 and volatilization. Natural sample ALV3352-7, which is unlikely tohave suffered Na loss to the same extent, has much lower D_{Na} (0.806).

Transition metals (Sc, Cr, Mn, Fe) and Mg

*D*s for Mg and transition metals increase with decreasing temperature (Sc, Mn, Fe) or are nearly constant (Mg, Cr). As expected D_{Fe} increases strongly with increased fO_2 (Phinney 1992; Wilke and Behrens 1999). A similar, but less marked increase is seen for D_{Cr}. D_{Sc} shows much smaller variations with fO_2, in accordance with its single valence state. No set of run experiments performed at the same temperature have a complete data set for Sc values under all three fO_2 (see Table 5); however, at 1,200°C D_{Sc} averages 0.016, which is exactly the same averaged value for both runs under more reducing conditions (IW) across the two highest isotherms (1,220 and 1,200°C). A strong increase of D_{Sc} with decreasing temperature occurs at oxidizing conditions, from 0.035 (1,220°C) up to 0.114 (1,180°C); see Fig. 3. Sample ALV-3352-7 with D_{Sc} of 0.021 is very close to the values at 1,180°C and QFM conditions; i.e., runs 25 (0.025) and 34 (0.021), respectively. Values of D_{Cr} are quite low with large uncertainty; however, excluding run 25 (1,180°C), D_{Cr} increases from 0.019 to 0.064 with increasing fO_2 (Fig. 3), possibly reflecting a smooth variation in the ratio of Cr^{2+} to Cr^{3+}. Average D_{Cr} close to IW conditions at 1,200 and 1,220°C (0.038) matches D_{Cr} in ALV-3352-7 (0.035). In air D_{Mn} increases with decreasing temperature—from 0.034 (1,220°C) to 0.184 (1,180°C), and increases sharply in the 1,180°C set of experiments: from 0.026 (QFM) to 0.184 (air). It is uncertain from our data if this increase is related to a departure from the dominant species Mn^{2+}. Natural sample ALV-3352-7 has the same D_{Mn} value (0.029) as run 31 at 1,220°C close to the QFM buffer. D_{Fe} values displayed in Fig. 3 show clearly both the effects of temperature (parallel trends) and oxygen fugacity (vertical trends). The strongest effect of temperature can be seen at air conditions, where D_{Fe} increases with decreasing temperature; 0.237 (1,220°C)–0.339 (1,200°C)–0.665 (1,180°C). However, at both IW and QFM conditions the influence of temperature is not apparent (Fig. 3). These results are in agreement with the previous studies of Sato (1989) and Phinney (1992) at similar temperatures. Thus, D_{Fe} is tightly constrained at 0.0267 ± 0.0047 under highly reducing conditions, where it is independent of temperature. In contrast D_{Fe} at air conditions varies greatly with temperature- reflecting the redox change from Fe^{2+} to Fe^{3+}. Sample ALV-3352-7 with D_{Fe} of 0.046 is situated

Table 5 Average partition coefficients

Temp (°C)	1,220						1,200						1,180							
Run no.	16		28		29		17		31		33		35		25		34		36	
log fO_2	–11.68		–8.18		–0.68		–11.93		–8.41		–0.68		–12.19		–8.65		–8.55		–0.68	
	D[a]	σ[b]	D	σ	D	σ	D	σ	D	σ	D	σ	D	σ	D	σ	D	σ	D	σ
Li	<0.367		<3.212		<0.816		<0.37		0.294	0.128	<2.050		<1.139		<0.306		0.575	0.183	0.678	
Mg	0.039	0.003	0.050	0.009	0.037	0.005	0.024	0.005	0.038	0.005	0.050	0.009	0.048	0.005	0.052	0.012	0.041	0.002	0.053	0.004
K	0.220	0.028	0.173	0.002	0.169	0.011	0.099	0.011	0.203	0.019	0.205	0.016	0.264	0.041	0.236	0.053	0.234	0.036	0.245	0.034
Sc	0.016	0.002	<0.077		0.035	0.003	0.015	0.003	0.016	0.005	<0.067		<0.017		0.024	0.003	0.021	0.002	0.114	0.036
Ti	0.039	0.002	0.047	0.014	0.034	0.008	0.014	0.008	0.038	0.003	0.052	0.010	0.038	0.007	0.047	0.010	0.041	0.002	0.123	0.052
Cr	0.038		<0.299		<0.274		0.037		0.045		<3.121		<0.030		0.365		0.019	0.004	0.064	0.025
Mn	0.027	0.002	0.043	0.009	0.034	0.003	0.020	0.003	0.029	0.004	0.040	0.009	0.034	0.006	0.054	0.014	0.026	0.001	0.184	0.065
Fe	0.023	0.002	0.146	0.017	0.237	0.031	0.032	0.031	0.115	0.005	0.339	0.015	0.025	0.003	0.123	0.014	0.086	0.007	0.665	0.068
Rb	<0.093		<0.676		<0.143		<0.097		0.114		<0.393		<0.154		1.217		0.058	0.003	0.122	
Sr	1.715	0.009	1.565	0.038	1.420	0.061	1.431	0.061	1.629	0.029	1.617	0.059	1.738	0.067	1.640	0.048	1.714	0.048	1.568	0.113
Y	0.008	0.001	<0.012		0.008		0.007		0.008	0.003	0.027	0.004	0.008	0.001	0.008	0.001	0.006	0.001	0.009	0.002
Zr	0.003	0.001	0.022		0.032		0.001		0.001		0.018		0.004		0.003	0.001	0.001	0.000	0.009	
Nb	<0.029		<0.336		0.114		<0.025		0.097		<0.245		<0.051		0.039		<0.017		0.139	
Cs	<0.771		<7.134		3.838		<0.780		0.596		<5.136		<3.284		<1.262		<1.074		<1.093	
Ba	0.301	0.046	0.226		0.213	0.028	0.129	0.028	0.247	0.049	0.360	0.007	0.340	0.068	0.244	0.039	0.327	0.058	0.277	0.054
La	0.065	0.004	0.084		0.049	0.012	0.027	0.012	0.077	0.018	0.079		0.059	0.008	0.059	0.009	0.061	0.009	0.071	0.021
Ce	0.049	0.006	0.044		0.037	0.008	0.031	0.008	0.054	0.014	0.040	0.002	0.051	0.010	0.061	0.015	0.045	0.004	0.045	0.008
Pr	0.049	0.007	<0.133		0.053		0.027		0.042	0.005	0.192		0.057	0.018	0.057	0.017	0.035	0.007	0.133	0.049
Nd	0.040	0.005	<0.144		0.040		0.025		0.054	0.017	0.112	0.007	0.039		0.031	0.004	0.033	0.006	0.104	
Sm	<0.044		<0.428		0.112	0.010	<0.025	0.010	0.081		<0.295		<0.075		0.033		0.037		<0.065	
Eu	0.869	0.084	0.242	0.072	0.117		0.260		0.109	0.037	<0.211		0.966	0.113	0.098	0.024	0.112	0.012	0.156	
Gd	<0.03		<0.348		<0.089		<0.031		0.042	0.012	<0.217		<0.05		0.071		0.021	0.004	0.153	0.015
Tb	<0.029		<0.268		<0.060		<0.012		0.028	0.010	0.237		<0.055		0.037	0.004	0.016	0.003	0.102	
Dy	<0.017		<0.137		0.115		0.024		0.049	0.016	<0.089		<0.0245		0.015		0.012	0.003	0.128	
Ho	<0.02		<0.13		0.077		<0.017		0.052	0.008	<0.101		<0.019		0.041	0.002	0.020	0.010	0.106	
Er	<0.024		<0.358		<0.088		<0.030		0.057	0.010	<0.20		<0.047		0.035		<0.015		0.137	
Tm	<0.049		<0.38		<0.098		<0.020		0.061		<0.26		<0.093		0.033		<0.025		0.122	
Yb	<0.03		<0.328		0.093		<0.028		<0.025		<0.23		<0.082		0.037		<0.017		0.141	
Lu	<0.024		<0.309		<0.101		<0.042		<0.024		<0.271		0.045		<0.023		<0.024		0.190	
Hf	<0.026		<0.328		<0.090		<0.027		<0.033		<0.259		0.057		0.036		<0.0157		0.153	0.051
Ta	0.042		<0.221		<0.064		<0.021		0.075	0.020	<0.174		<0.035		0.031	0.013	<0.012		0.170	
Pb	2.453		<12.64		0.989	0.200	1.521	0.200	1.592		<2.33		<4.87		0.553		2.533	0.697	2.721	0.485
Th	<0.173		<1.016		<0.340		<0.151		0.305	0.081	<0.833		<0.270		<0.082		<0.091		0.382	0.259
U	<0.43		<1.934		<0.182		<0.173		<0.12		0.501		<0.571		<0.050		<0.198		0.105	
Eu/Sr	0.507	0.049	0.155	0.046	0.083	0.004	0.182		0.067	0.023			0.556	0.068	0.060	0.015	0.065	0.007	0.099	0.007
Fe/Mg	0.60	0.07	2.93	0.62	6.39	1.23	1.32	1.32	3.02	0.39	6.80	1.22	0.51	0.08	2.35	0.59	2.11	0.21	12.47	1.52

[a] Upper limits are based on 3σ

[b] Error on D_i given as 1σ whenever calculation was possible

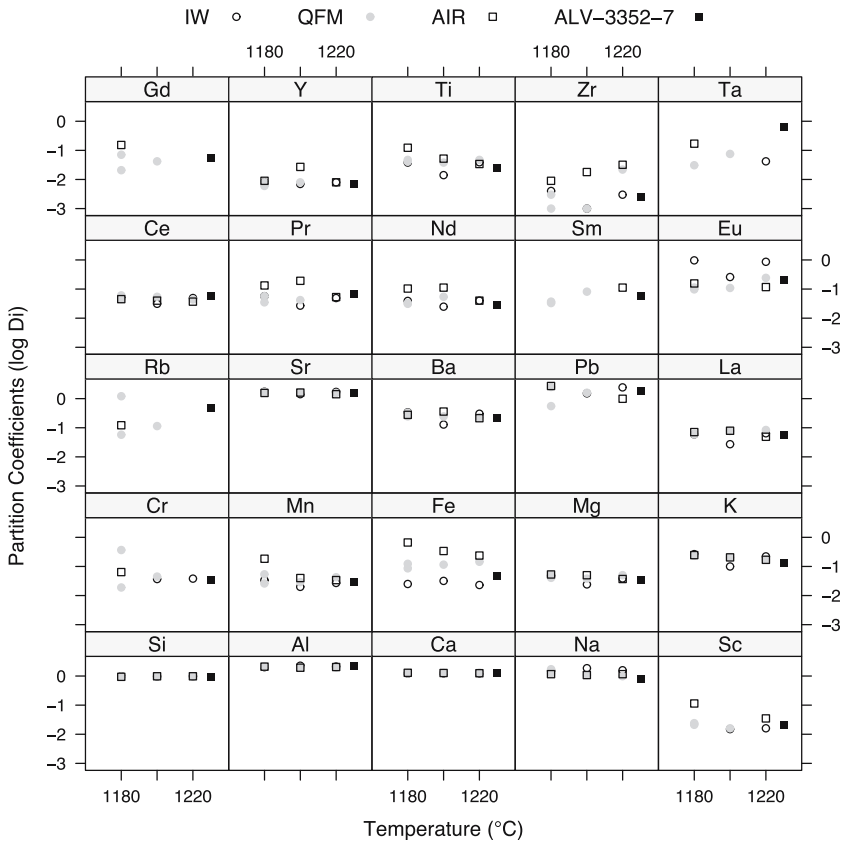

Fig. 3 Partition coefficients (log scale) of selected trace elements as a function of temperature for each oxygen fugacity studied. Also shown are the partition coefficients for natural sample ALV-3352-7 (Table 1)

between conditions intermediate to the IW and QFM buffers. D_{Mg} is well constrained with an overall average of 0.043 ± 0.009, showing neither great variation with temperature nor oxygen fugacity. Some subtle temperature effects at air conditions are observed; from 0.037 (1,220°C) down to 0.053 (1,180°C) as also reported in Bindeman et al. (1998). Peters et al. (1995) and Simon et al. (1994) reported partition coefficients of 0.035 and 0.039 for D_{Mg} using CAI bulk compositions. Using a similar bulk composition to this study, Sato (1989) and Phinney (1992) report values for D_{Mg} of 0.043 at 1,200°C and 0.044 at 1,180°C. Runs 29 (air at 1,220°C) and 31 (QFM at 1,200°C) with D_{Mg} values of 0.037 and 0.038, respectively, are close to 0.033 of natural sample ALV-3352-7.

Li and LILE (K, Rb, Sr, Cs, Ba, Pb)

Large ion lithophile elements (LILE) consist of strong compatible (Sr and Pb) to moderately incompatible (K, Rb, Ba) elements (Fig. 3). Thermal dependence may be strong (K, Pb), subtle (Ba), or practically absent (Sr). Li, Rb and Cs are highly variable and not well-constrained (Table 5). At air conditions, D_K increases with decreasing temperature—0.169 at 1,220°C to 0.245 at 1,180°C. Run no. 17 (1,200°C/IW) is low compared to the general trend. Average D_K calculated irrespective of temperature and fO_2 is 0.205 ± 0.048. Pairs of glass/plagioclase in sample ALV-3352-7 have D_K of 0.127, which is quite low when compared to any experimental result; the nearest being run no. 29 at 1,220°C/air (0.169). D_{Sr} is strongly compatible and very tightly constrained in our experiments—1.60 ± 0.1 independent of oxygen fugacity and temperature, reflecting our narrow range of temperature, liquid and plagioclase composition, parameters well known to influence the partitioning of Sr (Blundy and Wood 1991; Bindeman et al. 1998; Morse 1984). For comparison the value of D_{Sr} calculated for An_{77} at 1,200°C using the model of Blundy and Wood (1991) is 1.66, in good agreement with the value determined here. D_{Ba} is moderately incompatible with average values around 0.266 ± 0.069 independent of both temperature and fO_2. There is a small increase in D_{Ba} with decreasing temperature close to the QFM buffer; from 0.226 (1,220°C) up to 0.286 (1,180°C). Data for run 17 (IW) is unusually low compared to all other values. Run no. 29 (1,220°C/air) has D_{Ba} = 0.213, which is near the ALV-3352-7 D_{Ba} value of 0.2095. For comparison the value of D_{Ba} calculated for An_{77} at 1,200°C using the model of Blundy and Wood (1991) is 0.21, in excellent agreement with the value determined here. D_{Pb} is

compatible for almost the entire experimental range studied. Unfortunately, there is no complete set of values for D_{Pb} for any one oxygen fugacity condition. One trend is discernible though; D_{Pb} increases in air from 0.989 (1,220°C) to 2.72 (1,180°C), a pattern also observed in Bindeman et al. (1998). D_{Pb} of 1.901 from sample ALV-3352-7 is only closest to run no. 31 at 1,200°C/QFM (1.59).

Rare earths elements and Y

D_{REE} are reasonably constrained for the light REE (LREE), whereas Eu shows more complex behavior, due to its variable oxidation state. On the other hand, D values for middle and heavy REE (Sm, Gd, Tb, Dy, Ho, Er, Tm, Yb, Lu) are highly uncertain as their concentrations lie close to detection limits (Table 5). D_{La} and D_{Ce} have average values of 0.063 ± 0.017 and 0.046 ± 0.009, respectively. Natural sample ALV-3352-7 has D_{La} of 0.056, close to the average of runs 25 and 34 (1,180°C/QFM). $D_{Pr}$and D_{Nd} show a greater variability than D_{La} and D_{Ce}. Considering only the more robust subset of the data, with low standard deviations, average D_{Nd} is values are around 0.04, which is close to sample ALV-3352-7 value of 0.029. The exception is run 33 in air which has anomalously high D_{Pr} and D_{Nd}. The reason for this is not known. D_Y is consistently 0.008, irrespective of temperature or fO_2. D_Y for sample ALV-3352-7 is almost ten times higher (0.070) than the experimental value. D_{Eu} show clear trends of both effect of temperature and oxygen fugacity (Fig. 3). With a reversed pattern to that seen in D_{Fe} (Figure 3), the higher D_{Eu} values appear under the most reducing conditions; IW—Fig. 3. Notwithstanding the below-detection value for run 31 (1,200°C/air) and the anomalously low value of run 17, D_{Eu} averages 0.91 (IW), 0.14 (QFM) and 0.14 (air) independently of temperature. This reflects the well-established greater compatibility of Eu^{2+}, which has an ionic radius similar to Sr, relative to Eu^{3+} in plagioclase and the higher Eu^{2+}/ Eu^{3+} under reducing conditions. In a later section we will discuss the relative influences of crystal and melt composition, fO_2 and temperature on the behavior of D_{Eu}. At this point, however, we note that D_{Eu} for natural sample ALV-3352-7 (0.21) is close to the run 28 (1,220°C/QFM) value of 0.24.

HFSE (Ti, Zr, Nb, Hf, Ta, Th, U)

High field strength elements (HFSE) are highly incompatible in plagioclase. Except for Ti and Zr, the data are highly variable and elements are at their detection limits (Table 5). D_{Ti} shows temperature variations at air conditions (Fig. 3) similar to those seen in other transition metals; i.e., D_{Ti} increases with decreasing temperature—0.034 (1,220°C) to 0.123 (1,180°C). Close to QFM, D_{Ti} averages 0.043 ± 0.005 being in close in agreement with the experiments of Peters et al. (1995), who point to the possible presence of small amounts of Ti^{3+} under these conditions. On the other hand, Phinney (1992) found no such variation in D_{Ti} even with fO_2 ranging over 13 orders of magnitude. Bindeman et al. (1998) reported an increase in D_{Ti} with decreasing X_{an}. D_{Ti} from run no. 17 (1,200°C/IW) is very low (0.014) compared to both other runs under the same fO_2 that average 0.0385. Natural sample ALV-3352-7 D_{Ti} is intermediate (0.024) between these two values. D_{Zr} shows the greatest variation in partition coefficients for plagioclases (Fig. 3). Contrary to Ti, D_{Zr} at air conditions decreases with decreasing temperature, from 0.032 (1,220°C) down to 0.009 (1,180°C). At both 1,220 and 1,200°C isotherms, D_{Zr} is relatively constant at all oxygen fugacities— run no. 25 (1,180°C/QFM) with D_{Zr} of 0.003 is closest to sample ALV-3352–7 (0.0025). The variability of D_{Zr} in experiments run in air is strikingly similar to that for Fe (Fig. 3), despite the fact that Zr is only known as Zr^{4+}. D_{Ta} increases with decreasing temperature (Fig. 3); however, the experiments used to determine D_{Ta} are all three at different fO_2 conditions—0.042 (1,220/IW), 0.053 (1,200/QFM), and 0.170 (1,180/air). Natural sample ALV-3352-7 has D_{Ta} much higher (0.643) than any experimental run.

Discussion

Naturally occurring plagioclase can incorporate a wide range of elements and many geochemically important minor and trace elements (e.g., Li, K, Sr, Ba) are known to substitute for major divalent cations in the large octahedral A-site; however, a small number of elements (e.g., Ti, Zr) are thought to enter the tetrahedral site via coupled substitution by replacing Al. Others, such as Mg and Fe might be split between both A- and T-sites. Elements at very low concentrations are believed to partitioned into defect sites (e.g., Urusov and Dudnikova 1998).

D and site occupancy

The ideal formula of plagioclase represented by AT_4O_8, and with cation ordering in both A- and

T-sites, is rather complex. In previous studies, (see Bindeman and Davis 2000, and references therein) various end-member plagioclases have been synthesized and demonstrate a wide range of possible substitution mechanisms for minor and trace elements in plagioclase; e.g., coupled A- and T-site substitutions, six- to nine-coordinated A-sites. Stoichiometric deficiencies caused vacancy substitution on the A-site are thought to play an important role in plagioclases crystallizing from silica-rich melts (Longhi et al. 1976). Cation site occupancies of major elements in plagioclase (e.g., Si, Al, Ca, Na) are well established (e.g., Smith and Brown 1988), and general consensus for the cation site-assignments for most of the minor and trace elements should be: $VIII_A$: LILE (e.g., K^+), Na^+, Ca^{2+}, transition metals (e.g., Fe^{2+}, Sc), Mg^{2+}, REE^{3+} IV_T: transition metals (e.g., Fe^{3+}, Cr^{3+}), Mg^{2+}, HFSE (e.g., Ti^{4+}, Zr^{4+}), REE^{3+}, Al^{3+}, Si^{4+}. One the other hand, we can make no distinction between the different cavities in the A- and T-sites—i.e., A_1, A_2; T_1O, T_1 m, T_2O. Moreover, the site occupancies for some elements; e.g., the highly incompatible elements are particularly difficult to establish, since some of the elements shows heterovalent substitution (e.g., Fe and Eu) and/or site splitting (e.g., Mg and Fe). Figure 4 shows the relationship between ionic radius and several partition coefficients in terms of an Onuma-diagram (Onuma et al. 1968) for run no. 31 (1,200°C/QFM). The partitioning behaviour of the divalent cations Mg^{2+}, Fe^{2+}, Ca^{2+}, Sr^{2+}, Pb^{2+} and Ba^{2+} can be described by a parabola with a maximum that corresponds to the size of the VIII-fold coordinated A-site in plagioclase (Blundy and Wood 1994). Relative to this curve, all large cations with 3+ (e.g., REE) or 4+ valence are displaced to lower *D* values, while alkali metals, Li, Na, K, Pb, describe a more open parabola, consistent with lower solution energies for 1+ cations relative to higher valence cations of the same ionic radius (Blundy and Wood 1994, 2003a). On the other hand, small highly-charged ions (Sc^{3+}, Ti^{4+}, Cr^{3+}, Nb^{5+}, Ta^{5+}, Zr^{4+}) deviate significantly from the A-site parabolae and appear to lie closer to the size of IV-coordinated T-site, occupied by Al^{32+} and Si^{4+} (Fig. 4). There are some peculiarities, as in the case of Eu and Fe—both plotted as both 2+ and 3+ ionic radii. Eu is strongly affected by oxygen fugacity (see below) and shows its non-conformity within the LREE and Y trend. For Fe and Mg several authors, on the grounds of stoichiometry and experiments, have suggested tetrahedral occupancy (Bryan 1974; Longhi et al. 1976; Meyer and Shibata 1990; Sclar and Benimoff 1980; Sclar and Kastelic 1979; Zeng 1985; Murakami et al. 1992; Wenk et al. 1973; Wenk and Wilde 1973). Others showed that Fe^{2+} substitutes for the larger eight-coordinated A-sites as well, either by correlating ionic radius with *D* (Bindeman et al. 1998; Blundy 1997) or by using different spectroscopy techniques (Schümann and Hafner 1972; Hofmeister and Rossman 1984). Generally, our data at the QFM buffer for Fe and Mg seems to plot well within the 2+ parabola for the VIII-fold A-site (Fig. 4).

Lattice strain model (LSM)

Variation in pressure, temperature, fO_2, composition, crystal chemistry and liquid structure might all affect plagioclase partition coefficients. Predictive models based on experimental studies for the partitioning of plagioclase- melt pairs for the highly incompatible elements (i.e., Fe, Ti and Mg) have either shown strong partition coefficient relation to the liquid phase (e.g., Peters et al. 1995), or to the plagioclase composition (e.g., Bindeman et al. 1998). Additionally, in the case of partitioning of polyvalent cations (e.g., Fe, Eu), oxygen fugacity plays an important role (e.g., Phinney 1992; Wilke and Behrens 1999). Furthermore, Bindeman and Davis (2000); Bindeman et al. (1998) have shown for various trace elements that the plagioclase

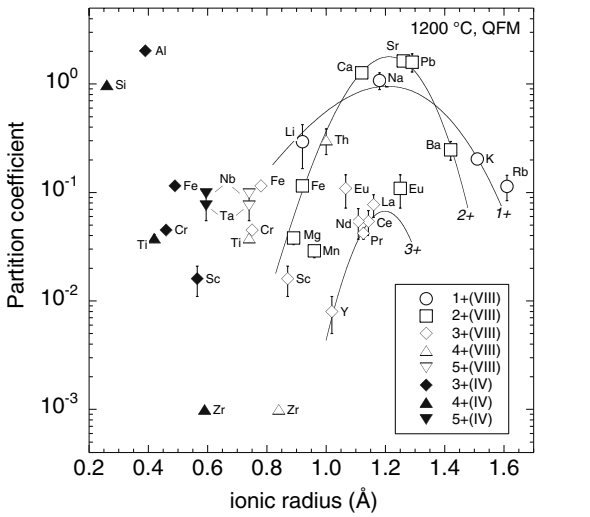

Fig. 4 Onuma diagram for run 31 (1,200°C/QFM) partition coefficients for 1+, 2+, 3+, 4+ and 5+ cations entering the plagioclase VIII-fold A-site and IV-fold T-site. Curves show nonlinear weighted least-square parabolic fits to Eq. 1 for 1+, 2+ and 3+ cations entering the A-site. Eu and Fe are plotted for both 2+ and 3+ valence states. The position of these cations relative to the parabola suggests that both elements are dominantly 2+. Sc, Cr, Fe^{3+}, Ti, Zr, Nb and Ta are plotted as both IV and VIII co-ordination. The position of these cations relative to the A-site parabolae suggests that all occur preferentially on the T-site. One SD error bars are only shown if larger than symbol. Ionic radii from Shannon (1976), except Nb_{IV}, Ta_{IV}, Sc_{IV}, Zr_{IV} and Cr_{IV}, which are extrapolated from higher co-ordination number radii

structure was primarily responsible for the difference in Ds at different concentrations.

Blundy and Wood (1994, 2003b) have rationalized the partitioning behaviour of homovalent series of cations between plagioclase and melt in terms of a Lattice Strain Model (LSM) based on the Brice (1975) equation which relates the partition coefficient of element $i(D_i)$, with radius r_i, to that of an element o (D_0) which has the same ionic radius r_0 as the crystallographic site of interest, such as the plagioclase A-site:

$$D_i = D_0 \exp\left(\frac{-4\pi E N_A\left(\frac{r_o}{2}(r_i - r_o)^2 + \frac{1}{3}(r_i - r_o)^3\right)}{RT}\right) \quad (1)$$

where N_A is Avogadro's number, E is the Young's Modulus of the site, R is the gas constant and T is in K. E, r_0 and D_0 can be obtained by fitting the experimental partitioning data for homovalent cation series to Eq. 1. Because of the rapid increase in apparent site Young's Modulus, E, with increasing cation charge and decreasing site dimensions (Blundy and Wood 2003a), this exercise is best confined to the large plagioclase A-site. In Fig. 5a we show an Onuma diagram of partition coefficients for selected large divalent cations and REE at 1,220°C and IW buffer. Ba, Sr, Ca and Mg lie along a smooth parabolic curves fitted as a function of their radii to Eq. 1. Values of $D_{0(2+)}$, $r_{0(2+)}$ and $E_{0(2+)}$ are displayed in Table 6, and are similar for all runs along a given isotherm. Individual experiments are consistent with those divalent elements occupying the A-site with optimal size $r_{0(2+)}$ of 1.203–1.225 Å. For comparison the calculated $r_{0(2+)}$ for An$_7$7 plagioclase from Blundy and Wood (2003b) is 1.214 Å. Our calculated $E_{(2+)}$ values (Table 6) lie in the range 104–124 GPa, again in good agreement with the model value of Blundy and Wood (2003b), 116 GPa.

We have also fitted 3+ parabolae to the partition coefficients of Y, La, Ce, Pr and Nd (Fig. 5a; other D_{REE} are too imprecise to be of use in fitting) to derive $E_{(3+)}$ and $r_{0(2+)}$ (Table 6). The fit parameters are subject to considerable uncertainty. However, fitted values of $E_{(3+)}$ are in the range 172–296 GPa, compared to a model value of 210 GPa (Blundy and Wood 2003b), and $r_{0(3+)}$ are in the range 1.15–1.22 Å, compared to 1.185 Å for An_{77} (Blundy and Wood 2003b).

The behaviour of D_{Fe} as a function of fO_2 can also be rationalized in terms of the LSM. At IW D_{Fe} lies below the 2+ parabola (Fig. 5a). With increasing fO_2, D_{Fe} increases (Fig. 5b), lying close to the 2+ parabola at QFM (see also Fig. 4), and significantly above the 3+ parabola in air (Fig. 5b). The higher value of D_{Fe} in air can be ascribed to incorporation of significant Fe^{3+} onto the tetrahedral site. The lower value of D_{Fe} at IW

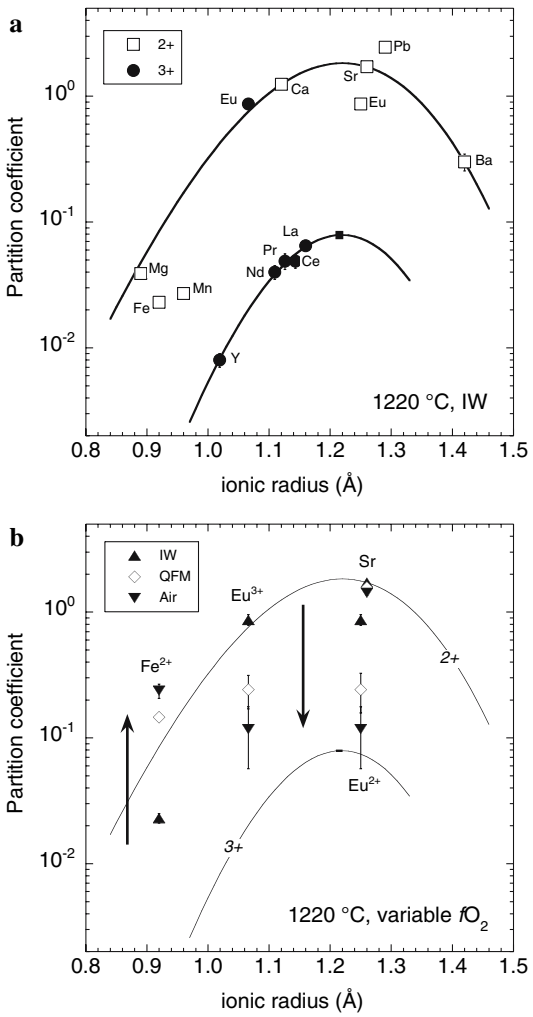

Fig. 5 Comparison of D values for runs at 1,220°C and three different oxygen fucacities. **a** D values for 2+ and 3+ cations from run 16 (IW buffer). Curves are fits to Lattice Strain Model (Eq. 1, fit parameters in Table 6). Note that D_{Pb} lies slightly above the 2+ parabola, while D_{Fe} and D_{Mn} lie slightly below. D_{Eu} lies close to D_{Sr} under these very reducing conditions, because of the predominance of Eu^{2+} over Eu^{3+}. **b** Effect of fO_2 on D_{Eu} and D_{Fe}. The curves denote the 2+ and 3+ parabolae from **a** the position of these curves is very similar in all three runs at 1,220 °C as evinced by the near-constant D_{Sr}. The *arrows* show the effect of increasing fO_2 from IW to air. D_{Eu} is progressively displaced towards the 3+ parabola as the Eu^{2+}/Eu^{3+} ratio in the melt decreases. D_{Fe} shows the opposite behaviour. At QFM D_{Fe} lies close to the 2+ parabola, suggesting that this is the dominant species in the melt. In air D_{Fe} is displaced above the 2+ parabola, due to incorporation of significant Fe^{3+} onto the T-site. The displacement of D_{Fe} to lower values in the IW experiment may reflect the presence of significant Fe_0 in the melt under such reducing conditions (cf. Schreiber 1986). One SD *error bars* as in Fig. 4. Ionic radii from Shannon (1976)

Table 6 Fit parameters from Lattice Strain Model

Run no	31 QFM	35 IW	34 QFM	36 AIR	16 IW	17 IW
Valence	2+	2+	2+	2+	2+	2+
D_0	1.82 (3)	1.827 (2)	1.867 (4)	1.795 (4)	1.833 (9)	1.73 (5)
E_0	120 (5)	104 (1)	113 (3)	108 (3)	110 (2)	140 (6)
r_0	1.212 (2)	1.225 (1)	1.219 (3)	1.212 (4)	1.220 (1)	1.203 (3)
Valence	3+	3+	3+	3+	3+	3+
D_0	ND	0.058 (7)	ND	ND	0.079 (29)	0.029 (1)
E_0	ND	296 (202)	ND	ND	172 (77)	282 (79)
r_0	ND	1.163 (29)	ND	ND	1.219 (58)	1.145 (11)

All calculations made for plagioclase A-site

Values in parentheses are 1 SD uncertainties on the fit parameters in terms of least significant figures

D_0 strain-compensated partition coefficient

E Young Modulus of the lattice site (in GPa)

r_0 Optimum site radius (in Å)

is suggestive of the presence of some Fe_0 in the melt (cf. Schreiber 1986). The presence of Fe^{3+} on the T-site is supported by our preliminary SREF investigations (Aigner-Torres 2003).

Partitioning behaviour of Eu

The LSM provides a quantitative framework for understanding the partitioning behaviour of Eu, which occurs as both 2+ and 3+ cations, depending on fO_2. If all Eu is present as Eu^{3+} D_{Eu} will lie along the 3+ parabola defined by other, exclusively trivalent, REE (in-air run, Fig. 5b). Conversely if all Eu is present as Eu^{2+}, then D_{Eu} will lie along the 2+ parabola defined by Ca, Sr, Ba etc (IW run, Fig. 5b). The extent to which the real D_{Eu} deviates from both parabolae contains information on the Eu^{2+}/Eu^{3+} ratio in the melt, as previously noted by numerous workers. The virtue of the LSM approach, however, is that it can be used to constrain precisely $D_{Eu}2+$ and $D_{Eu}3+$ in a way not previously possible. Thus, most previous studies have been obliged to assume that $D_{Eu}2+ = D_{Sr}$, which is inconsistent with the slight difference in the ionic radii of these two cations (Shannon 1976).

Following Wilke and Behrens (1999) it is a simple matter to show that:

$$\left(\frac{Eu^{2+}}{Eu^{3+}}\right)_{melt} = \frac{D_{Eu^{3+}} - D_{Eu}}{D_{Eu} - D_{Eu^{2+}}} \quad (2)$$

where $D_{Eu}3+$ is the partition coefficient for Eu^{3+}, $D_{Eu}2+$ is the partition coefficient for Eu^{2+}, and D_{Eu} is the observed partition coefficient for mixed valence Eu. $D^3_{Eu}+$ and $D^2_{Eu}+$ can be calculated using the LSM, based on the measured partition coefficient of another REE^{3+} and Sr, respectively, using rearranged versions of Eq. 1, Blundy and Wood (1994):

$$D_{Eu^{2+}}(P,T,X) = D_{Sr}(P,T,X)\exp\left(\frac{-4\pi E_{2+}N_A\left[\frac{r_{0(2+)}}{2}(r^2_{Sr} - r^2_{Eu^{2+}}) + \frac{1}{3}(r^3_{Eu^{2+}} - r^3_{Sr})\right]}{RT}\right) \quad (3a)$$

$$D_{Eu^{3+}}(P,T,X) = D_{REE}(P,T,X)\exp\left(\frac{-4\pi E_{3+}N_A\left[\frac{r_{0(3+)}}{2}(r^2_{REE} - r^2_{Eu^{3+}}) + \frac{1}{3}(r^3_{Eu^{3+}} - r^3_{REE})\right]}{RT}\right) \quad (3b)$$

where $D_{Sr}(P,T,X)$ is the partition coefficient for Sr under the same pressure, temperature composition conditions, $D_{REE}(P,T,X)$ is the partition coefficient of another trivalent REE, ideally reasonably close in ionic radius to Eu^{3+}, e.g., Gd, Sm. Other parameters are defined as in Eq. 1. Both D_{Sr} and D_{REE} can be measured directly, or calculated using expressions in Blundy and Wood (1991) and Bindeman et al. (1998). Ionic radii for Eu^{2+}, Eu^{3+}, REE^{3+} and Sr^{2+} in VIII-fold co-ordination are taken from Shannon (1976). The values of $r_{0(2+)}$, $r_{0(3+)}$, $E_{(2+)}$ and $E_{(3+)}$ can be taken from Blundy and Wood (2003b) as follows:

$$r_{0(2+)}(\text{Å}) = 1.258 - 0.057X_{An} \quad (4a)$$

$$r_{0(3+)} = r_{0(2+)} - 0.03\text{Å} \quad (4b)$$

$$E_{2+} = 116\text{GPa} \quad (4c)$$

$$E_{3+} = 210\text{GPa} \quad (4d)$$

Note that these expressions effectively eliminate the influence of plagioclase crystal chemistry of Eu partitioning, by considering the effect of X_{An} on site radius and Young's Modulus.

We have used Eqs. 2–4 to calculate Eu^{2+}/Eu^{3+} for our 9 plagioclase partitioning experiments in addition to 82 published experiments from the following sources: Sun et al. (1974), Drake (1975), Weill and McKay (1975), McKay et al. (1994), Blundy (1997), Bindeman et al. (1998) and Wilke and Behrens (1999). In some of these studies (e.g., McKay et al. 1994; Blundy 1997) the partition coefficients of both Sr and another REE, in addition to Eu and the anorthite content of the plagioclase, were reported, making application of Eq. 3 straightforward. For the other studies we have had to estimate some of the key parameters, namely: for Drake (1975), D_{Ce} is taken from Drake and Weill's (1975) experiments at similar *P–T–X*; for Wilke and Behrens (1999) D_{Sr} is estimated from Blundy and Wood (1991) using reported An contents; for Sun et al. (1974) D^{3+}_{Eu} is estimated by extrapolating their linear Eq. 25 to high fO_2 (10^{-3}) where almost all Eu is trivalent.

Eu^{2+}/Eu^{3+} can be easily converted to Eu^{3+}/Eu_{tot}, the proportion of the total Eu in the melt that is trivalent, and this is plotted for all 91 experiments in Fig. 6. The data describe a sigmoidal trend, as observed in all previous studies, with the cross-over from dominantly Eu^{3+} to dominantly Eu^{2+} between $fO_2 = 10^{-10}$ and 10^{-13}. In detail, although all datasets show similar sigmoidal patterns, there is scatter suggesting that parameters in addition to fO_2 control Eu^{2+}/Eu^{3+}. These include temperature, pressure and melt composition.

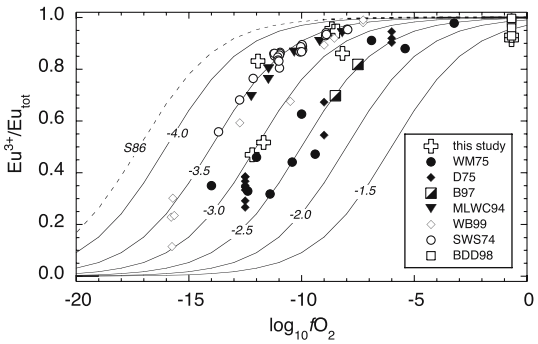

Fig. 6 Variation in Eu^{3+}/Eu_{tot} ratio as a function of fO_2 in melts coexisting with plagioclase for various experimental studies calculated according to Eq. 2–4. Data sources are: SWS74, Sun et al. (1974); D75, Drake (1975); WM75, Weill and McKay (1975); MLWC94, McKay et al. (1994); B97, Blundy (1997); BDD98, Bindeman et al. (1998); WB99, Wilke and Behrens (1999); and this study. The curved lines denote calculated variation in Eu^{3+}/Eu_{tot} labeled for different values of the reduction potential, E', as defined in Eq. 5. The curve labeled S86 denotes the curve for $E' = -4.3$ as determined for a synthetic melt by Schreiber (1986). The experimental data for geologically realistic melts are best described with E' in the range –3.5 to –2.5. Note that for melt more oxidizing than QFM+2 (fO_2~10^{-6}) over 90% of Eu is trivalent

Given that all of the experiments were conducted at 1 atmosphere, with the exception of Wilke and Behrens (1999), conducted at 500 MPa, we have insufficient data to investigate the effect of pressure. As the Wilke and Behrens (1999) show no appreciable offset relative to the 1 atm data, we suggest that the effect of pressure is negligible, consistent with the likely small difference in partial molar volume of Eu^{2+} and Eu^{3+} species in the melt. We will focus instead on temperature and melt compositional effects.

A useful parameter for exploring the role of temperature and melt composition of Eu redox equilibria is the standard redox potential, E', as defined by Schreiber (1986). E' is a measure of the reducibility of an ion pair relative to the equilibrium:

$$O_{2(gas)} + 4e^- = 2O^{2-}_{melt}$$

E' can then be defined as:

$$E' = \frac{1}{4}\log_{10} fO_2 + \log_{10}\left(\frac{Eu^{2+}}{Eu^{3+}}\right) \quad (5)$$

Thus, for any given melt composition, a plot of $\log_{10}(Eu^{2+}/Eu^{2+})$ versus $\log_{10} fO_2$ will yield a slope of –0.25 and an intercept E'. Such a plot is shown in Fig. 7. The slope of –0.25 is clearly evident for all suites of data points. However, the intercept, i.e., E', varies from suite to suite, indicating that melt composition and/or temperature also play a role. In effect, this is the cause of the scatter apparent in Fig. 6. We also note that for any given experimental suite, E' for experiments run in air is displaced to less negative values (Fig. 7).

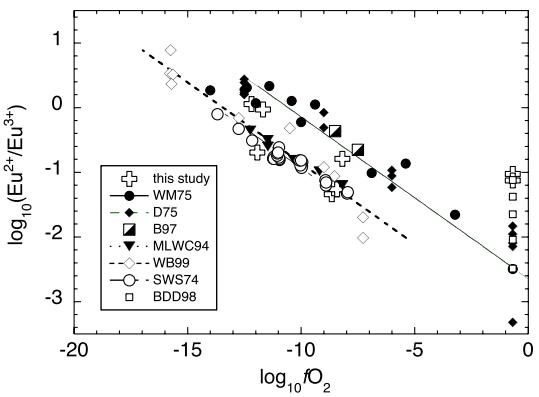

Fig. 7 Variation in $\log_{10}(Eu^{2+}/Eu^{3+})$ as a function of $\log_{10} fO_2$ for the same experimental data as Fig. 6. *Straight lines* denote different values of E', as defined in Eq. 5, fitted to individual datasets (*straight lines*). Note how in-air data for any given bulk composition are displaced to less negative values of E', due to melt structure changes resulting from oxidation of Fe^{2+} to Fe^{3+}

Schreiber (1986) determined E' for a synthetic borosilicate melt (57.9 wt% SiO_2, 1.0% TiO_2, 0.5% ZrO_2, 14.7% B_2O_3, 0.5% La_2O_3, 2.0% MgO, 17.7% Na_2O, 5.7% Li_2O) at 1,150°C to be –4.3. This is significantly more negative than E' for any of the experiments we have considered (Fig. 6) and consequently yields a sigmoidal pattern in that is displaced to lower fO_2 from that shown by the Eu partitioning data. Morris et al. (1974) and Morris and Haskin (1974) have also determined Eu^{2+}/Eu^{3+} ratios for a range of synthetic melt compositions, more geologically realistic than that of Schreiber (1986), at temperatures of 1,415–1,650 °C. Their values of E', calculated from Eq. 5, are in the range from –1.3 to –3.3 and show a strong correlation with melt composition (Fig. 8). If we exclude their $CaAl_2Si_2O_8$ melts, which yield unusually low E' values, their mean value of E' is –2.66 ± 0.35, which provides an excellent match to the plagioclase-melt Eu partitioning data, as shown in Fig. 6 and 7. A global fit to the Eu partitioning data in Fig. 7 yields E' is –3.00 ± 0.06 ($r^2 = 0.45$). Fits to specific datasets performed on a single bulk composition over a wide range of fO_2 (Fig. 7) yield slightly different values of E' with larger regression coefficients, e.g., Drake (1975), –2.65 ± 0.08 ($r^2 = 0.91$); Sun et al. (1974), –3.44 ± 0.02 (r^2=0.88); Wilke and Behrens (1999), –3.36 ± 0.08 ($r^2 = 0.93$); Weill and McKay (1975), –2.64 ± 0.09 ($r^2 = 0.90$).

The uncertainty in the global-fit E' reflects variations between experiments, which may be thermal or compositional in origin. Morris and Haskin (1974) have shown that the thermal dependence of E' is very small, decreasing by only 0.2 units from ~1,400 to ~1,600°C. Wilke and Behrens (1999) arrive at a similar conclusion. We conclude that melt composition exercises a greater control over the observed scatter in E' than does temperature. Although a full parameterization of E' in terms of melt composition is beyond the scope of this study, and would probably require a much greater range of melt composition than is available in our dataset, it is instructive in understanding the persistent deviation of the in-air experimental data from the trends shown by experiments under more reducing conditions (Fig. 7). We suggest that in air Fe in the melt is present almost exclusively as Fe^{3+}, rather than Fe^{2+}, which has a dramatic effect on melt structure and hence on E'. The Morris and Haskin (1974) and Morris et al. (1974) data show that as the molar ratio of Al + Si/O in the melt increases (Fig. 8), so E' becomes less negative. If we assume that Fe^{3+} has a similar structural role in the melt to Al^{3+} (e.g., Mysen et al. 1985), then the increase in Fe^{3+} under oxidizing conditions will have a similar effect to increasing Al + Si/O for any given melt composition, thereby making E' less negative. This is entirely consistent with the partitioning data in Fig. 7.

We conclude that, although Eu partitioning data can be used to extract E' for natural melts, the strong melt compositional effects on E' need further clarification before Eu partition coefficients between plagioclase and melt can be used as a robust oxybarometer for silicate melts. The issue is compounded by the fact that in natural Fe-bearing melts the influence of Fe^{3+} must also be accounted for, in a way that is not possible in the Fe-free experimental melts of Morris and Haskin (1974); Morris et al. (1974) and Schreiber (1986). Nonetheless, it is clear that once a suitable formalism for relating E' to melt chemistry is found, ideally through further experimental studies, plagioclase-melt partitioning can be used to quantify fO_2 in magmatic rocks that lack other means of oxybarometry, such as coexisting Fe–Ti oxides.

Petrogenetic implications for basaltic processes

The wide range of data presented here for D values for plagioclase enable us to attempt to evaluate the conditions of formation of our natural sample ALV-3372. Since our experimental runs have investigated a small temperature range (Fig. 3), we have averaged partition coefficients for each fO_2 across all three isotherms (1,200 ± 20°C). Average experimental Ds are then compared with the averaged calculated partition coefficients for the plagioclase-matrix glass pair from ALV-3372 (Table 1) on a spider-diagram (Fig. 9). For

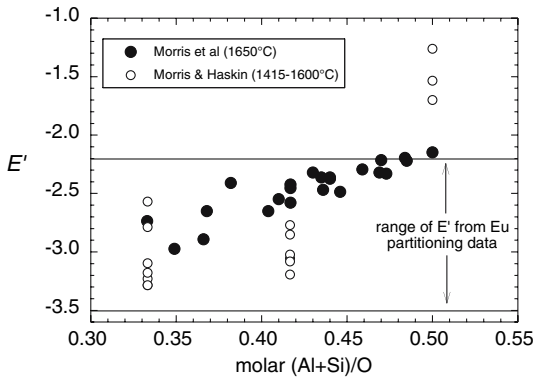

Fig. 8 Dependence of E' on melt composition, as expressed in terms of molar (Al + Si)/O, from isothermal experiments of Morris and Haskin (1974) and polythermal experiments Morris et al. (1974). For an Fe-bearing melt oxidation of Fe^{2+} to Fe^{3+} is likely to have a similar structural effect on the melt as increasing (Al + Si)/O and so making E' less negative as observed in Fig. 7. The *horizontal lines* denote the range of E' from Figs. 6 and 7

clarity, confidence intervals for averaged *D*s were calculated only under QFM conditions and are shown as error bars. Overall there is very good agreement between the experimental *D*s and those measured on the natural sample. Significantly, for all the elements that show multiple valence states, such as Eu, Cr, Fe, and possibly Ti, the natural ALV-3372 *D*values are intermediate between the averaged values for IW and QFM conditions.

An important feature of Fig. 9 is the change in the ratio of *D* value—i.e., Kd values—between Fe and Mg under varying redox conditions. For example, at the IW buffer, D_{Fe}/D_{Mg} is 0.8 ± 0.4, at QFM it is 2.6 ± 0.4, and in air it is 8.6 ± 3.4. The corresponding value for ALV-3372 is 1.40 ± 0.37, again suggestive of conditions between QFM and IW. The change in Fe–Mg fractionation cannot reflect temperature or plagioclase compositional variations, since both ranges are very small in our experiments. The ratio D_{Eu}/D_{Sr} is also strongly sensitive to fO_2, decreasing from 0.41 ± 0.20 at IW to 0.09 ± 0.05 at QFM and 0.09 ± 0.01 in air. The corresponding value for ALV-3372 is 0.13 ± 0.04. Based on a graphical comparison of the ALV-3372 data with the averaged experimental data for both $Kd_{Fe–Mg}$ and Kd_{Eu-Sr} we can constrain the fO_2 of the natural sample to be 0.9–1.8 log units below QFM (Fig. 10), in excellent agreement with the estimates of Pacific MORB fO_2 of Christie et al. (1986) based on ferric-ferrous determinations of basaltic glasses, 1.6 ± 0.5 log units below QFM. The calculated fO_2 for ALV-3372, using the modeling approach developed above, with an average E' of 3.24 ± 0.12 for our experiments at IW and QFM, yields fO_2 between QFM-1.2 and QFM-0.7. Evidently the combined fractionation of Eu^{2+}–Sr and Fe–Mg by plagioclase has considerable potential as an oxybarometer for natural magmatic rocks.

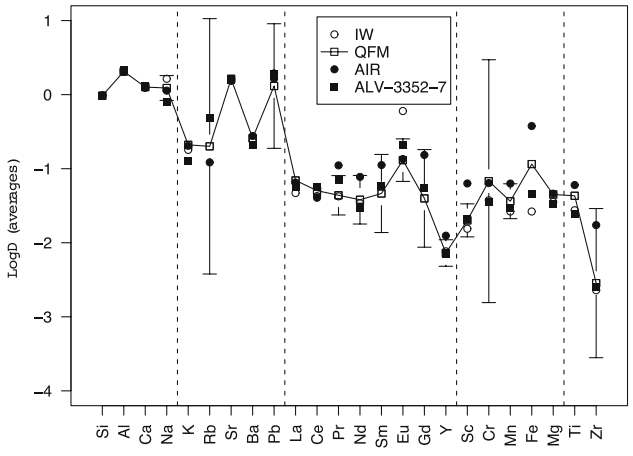

Fig. 9 Comparison of average experimental partition coefficients under different fO_2 conditions (Table 5) with natural plagioclase-matrix data from sample ALV-3352-7 (Table 1) plotted on an extended spider diagram. Confidence intervals (P = 0.95) only shown as *error bars* for QFM average. Note the strong fO_2-sensitive fractionation of Fe from Mg

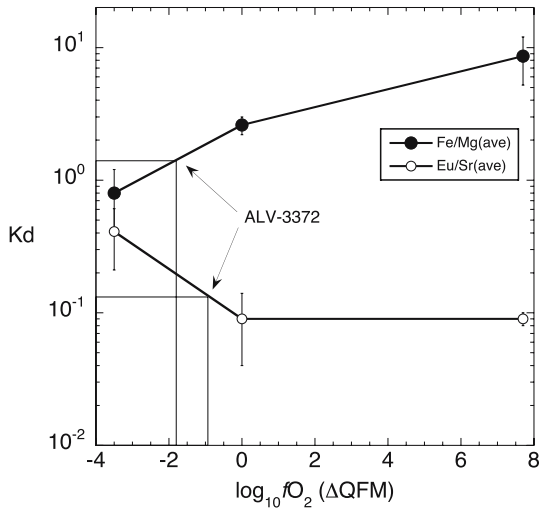

Fig. 10 Graphical estimation of fO_2 for natural sample ALV-3352-7 based on $Kd_{Fe–Mg}$ and $Kd_{Eu–Sr}$. The average experimental data (1,180–1,220°C) with 1 SD *error bars* are plotted as a function of fO_2 relative to QFM and connected with *straight lines*. The corresponding values for the plagioclase-matrix pair from ALV-3352-7 are interpolated between the QFM and IW data points to estimate fO_2

Conclusion

The experimental partitioning of up to 34 different trace elements between plagioclase and basaltic melts under high temperature magmatic conditions and over a wide range of oxygen fugacity was accurately measured by laser ablation ICP-MS and their partition coefficients reported and compared with some previous studies. The combined effect of temperature and oxygen fugacity produce relative minor changes in most D values, with a general tendency of increasing *D* with decreasing temperature, except for D_{Zr}. Partitioning data from divalent cations and REE on the large A-site of plagioclase are consistent with previous parameterizations using the lattice strain model. Overall, a wide range of new D values for several elements for plagioclase-bearing basaltic melts were determined and could be readily used for geochemical, modeling.

There is a significant change in plagioclase-melt partition coefficients for polyvalent elements Fe, Cr and Eu with oxygen fugacity and consequently for Kd values of pairs of elements such as Fe–Mg and Eu–Sr. The best match of the experiments to natural sample

ALV-3372 suggest that this magma equilibrated at conditions slightly more reducing than QFM.

Application of the lattice strain model to the partitioning of Eu provides a novel means of quantifying the Eu^{2+}/Eu^{3+} ratio of the coexisting melt more precisely than was previously possible. By augmenting our dataset with published data on plagioclase-melt partitioning of Eu we have been able to show that D_{Eu} is sensitive to both fO_2 and melt composition. This variability requires parameterization before the potential of Eu partitioning between plagioclase and melt as an oxybarometer can be realized. The melt compositional sensitivity of Eu^{2+}/Eu^{3+} ratios leads to a spread of fO_2 values over which D_{Eu} falls sharply due to the progressive oxidation of Eu^{2+} to Eu^{3+}. The data show that for the melt compositions studied (basalt to tonalite), this change occurs at fO_2 about 2 log units more oxidizing than the IW buffer. At conditions more oxidizing than QFM+2, the Eu^{2+}/Eu^{3+} ratio sufficiently low (less than 10% total Eu as Eu^{2+}; Fig. 6) that plagioclase will not generate significant Eu anomalies in derivative melts.

Acknowledgments M.A.-T. is indebted to the Swiss National Science Foundation for research grants and kindly thanks J. Sinton for providing the samples from the R/V Atlantis cruise 3–31. T. We thank T. Ntaflos from the University of Vienna for helping with the EMP analysis. JDB acknowledges a Senior Research Fellowship from the NERC. This paper is dedicated to the memory of Prof. V. Trommsdorff.

References

Aigner-Torres M (2003) Iron, magnesium and other highly incompatible elements partitioning between plagioclase and basaltic melts: an experimental and analytical approach. Ph. D. thesis Nr. 15026, ETH Zurich

Baker MB, Grove TL, Price R (1994) Primitive basalts and andesites from the Mt Shasta region, N. California: products of varying melt fraction and water content. Contrib Miner Petrol 118:111–129

Bartels KS, Kinzler RJ, Grove TL (1991) High pressure phase relations of primitive high-alumina basalts from Medicine Lake volcano, northern California. Contrib Miner Petrol 108:253–270

Bender A, Hodges FN, Bence AE (1978) Petrogenesis of basalts from the Project FAMOUS area. Earth Planet Sci Lett 41:277–302

Bindeman I, Davis A (2000) Trace element partitioning between plagioclase and melt: investigation of dopant influence on partition behavior. Geochim Cosmochim Acta 64(16):2863–2878

Bindeman I, Davis A, Drake M (1998) Ion microprobe study of plagioclase–basalt partition experiments at natural concentration levels of trace elements. Geochim Cosmochim Acta 62(7):1175–1193

Blundy J (1997) Experimental study of a Kiglapait marginal rock and implications for trace element partitioning in layered intrusions. Chem Geol 141:73–92

Blundy J, Wood B (1991) Crystal-chemical controls on the partitioning of Sr and Ba between plagioclase feldspar, silicate melts, and hydrothermal solutions. Geochim Cosmochim Acta 55:193–209

Blundy J, Wood B (1994) Prediction of crystal-melt partition coefficients from elastic moduli. Nature 372:452–454

Blundy J, Wood B (2003a) Partitioning of trace elements between crystals and melts. Earth Planet Sci Lett 210:383–397

Blundy J, Wood B (2003b) Mineral-melt partitioning of uranium, thorium and their daughters. In: Bourdon B et al (eds) Uranium-series geochemistry reviews in mineralogy vol 52, pp 39–123

Borisov A, Jones J (1999) An evaluations of Re, as an alternative to Pt, for the 1 bar loop technique: an experimental study at 1,400°C. Am Miner 84:1528–1534

Brice J (1975) Some thermodynamics aspects of the growth of strained crystals. J Cryst Growth 28:249–253

Bryan W (1974) Fe–Mg relationships in sector-zoned submarine basalt plagioclase. Earth Planet Sci Lett 24:157–165

Christie D, Carmichael I, Langmuir C (1986) Oxidation states of mid-ocean ridge basalt glasses. Earth Planet Sci Lett 79:397–411

Drake MJ (1975) The oxidation state of europium as an indicator of oxygen fugacity. Geochim Cosmochim Acta 39:55–64

Drake MJ, Weill DF (1975) Partition of Sr, Ba, Eu^{2+}, Eu^{2+} and other REE between plagioclase feldspar and magmatic liquid: an experimental study. Geochim Cosmochim Acta 39:689–712

Grove T (1981) Use of FePt alloy to eliminate the iron loss problem in 1 atmosphere gas mixing experiments: theoretical and practical considerations. Contrib Mineral Petrol 78:298–304

Grove TL, Bryan WB (1983) Fractionation of pyx-phyric MORB at low pressure. An experimental study. Contrib Mineral Petrol 84:293–309

Grove T, Baker M, Kinzler R (1984a) Coupled CaAl–NaSi diffusion in plagioclase feldspar: experiments and application to cooling rate speedometry. Geochim Cosmochim Acta 48:2113–2121

Grove TL, Baker MB, Kinzler RJ (1984b) Coupled CaAl-NaSi diffusion in plagioclase feldspar: experiments and applications to cooling rate speedometry. Geochim Cosmochim Acta 48:2113–2121

Grove TL, Kinzler RJ, Bryan WB (1990) Natural and experimental phase relations of lavas from Serocki Volcano. In: Detrick R, Honnorez J, Bryan WB, et al. (eds) Proceeding of the ocean drilling program, scientific results, vol 106. Ocean drilling program, College Station, TX, pp 9–17

Günther D, Frischknecht R, Heinrich C, Kahlert H (1997) Capabilities of an argon fluoride 193 nm excimer laser for laser ablation inductively coupled plasma mass spectrometry microanalysis of geological materials. J Anal Atomic Spectrom 12(9):939–944

Heinrich C, Pettke T, Halter W, Aigner-Torres M, Audètat A, Günther D, Hattendorf B, Bleiner D, Guillong M, Horn I (2003) Quantitative multi-element analysis of minerals, fluid and melt inclusions by laser-ablation inductively-coupled-plasma mass- spectrometry. Geochim Cosmochim Acta 67:3473–3496

Hofmeister A, Rossman G (1984) Determination of Fe^{3+} and Fe^{2+} concentrations in feldspar by optical absorption and EPR spectroscopy. Phys Chem Miner 11:213–224

Longerich H, Jackson S, Guenther D (1996) Laser ablation inductively coupled plasma mass spectrometric transient signal data acquisition and analyte concentration calculation. J Anal Atomic Spectrom 11:899–904

Longhi J, Walker D, Hays J (1976) Fe and Mg in plagioclase. Proceedings of Lunar Science Conference 7th, pp 1281–1300

McKay G, Le L, Wagstaff J, Crozaz G (1994) Experimental partitioning of rare earth elements and strontium: constraints on petrogenesis and redox conditions during crystallization of Antarctic angrite Lewis Cliff 86010. Geochim Cosmochim Acta 58:2911–2919

Meyer P, Shibata T (1990) Complex zoning in plagioclase feldspars from ODP site 648. In: Detrick R, Honnorez J, Bryan W, Juteau T (eds) Proceedings of ODP science results, vol 106/109, pp 123–142

Morris RV, Haskin LA (1974). EPR measurement of the effect of glass composition on the oxidation data of europium. Geochim Cosmochim Acta 38:1435–1446

Morris RV, Haskin LA, Biggar GM, O'Hara MJ (1974) Measurement of the effects of temperature and partial pressure of oxygen on the oxidation states of europium in silicate glasses. Geochim Cosmochim Acta 38:1447–1459

Morse S (1984) Cation diffusion in plagioclase feldspar. Science 225:504–505

Murakami H, Kimata M, Shimoda S, Ito E, Sasaki S (1992) Solubility of $CaMgSi_3O_8$ and Si_4O_8 endmembers in anorthite. J Miner Pet Econ Geol 87:491–509

Mysen BO, Virgo D, Neumann E, Seifert F (1985) Redox equilibria and the structural states of ferric and ferrous iron in melts in the system CaO–MgO–Al_2O_3–SiO_2–Fe–O: relationships between redox equilibria. melt structure and liquidus phase equilibria. Am Mineral 70:317–331

Onuma N, Higuchi H, Wakita H, Nagasawa H (1968) Trace element partition between two pyroxenes and the host lava. Earth Planet. Sci Lett 5:47–51

Peters M, Shaffer E, Burnett D (1994) Mg and Ti partition coefficients for anorthite-CAI liquid: dependence on oxygen fugacity and melt composition. Lunar Planet Sci XXV:1075–1076

Peters M, Shaffer E, Burnett D, Kim S (1995) Magnesium and titanium partitioning between anorthite and type B CAI liquid: dependence on oxygen fugacity and liquid composition. Geochim Cosmochim Acta 59(13):2785–2796

Pettke T (2006) In situ laser-ablation ICPMS analysis of melt inclusions and prospects for constraining subduction zone magmatism Mineralogical Association of Canada, Montreal, 36, pp 51–80

Pettke T, Halter WE, Webster JD, Aigner-Torres M, Heinrich CA (2004) Accurate quantification of melt inclusion chemistry by LAICPMS: a comparison with EMP and SIMS and advantages and possible limitations of these methods. Lithos 78:333–361

Phinney W (1992) Partition coefficients for iron between plagioclase and basalt as a function of oxygen fugacity: implications for archean and lunar anorthosites. Geochim Cosmochim Acta 56:1885–1895

Phinney W (1994) FeO and MgO in plagioclase of lunar anorthosites: igneous or metamorphic? Lunar Planet Sci XXV:1081–1082

Sano T, Fujii T, Deshmukh SS, Fukuoka T, Aramaki S (2001) Differentiation processes of Deccan Trap basalts: contribution from geochemistry and experimental petrology. J Petrol 42:2175–2195

Sato H (1989) Mg–Fe partitioning between plagioclase and liquid in basalts of hole 504B, ODP Leg 111: a study of melting at 1 atm. In: Becker K, Sakai H et al (eds) Proceedings of the ocean drilling project, scientific results, vol 111, pp 17–26

Schreiber HD (1986) Redox processes in glass-forming melts. J Non Cryst Solids 84:129–141

Schümann K, Hafner S (1972) On the amount of ferric iron in plagioclases from lunar igneous rocks. Geochim Cosmochim Acta 1:615–621

Sclar C, Benimoff A (1980) Magnesium in anorthite: synthesis and petrological significance of the $CaMgSi_3O_8$ series. EOS Am Geophys Union 61:392

Sclar C, Kastelic R (1979) Iron in anorthite: synthesis and characterization of the $CaAl_2$ Si_2O_8–$CaFeSi_3O_8$ series. EOS Am Geophys Union 60:421

Shannon B (1976) Revised effective ionic radii and systematic studies of interatomic distances in halides and chalcogenides. Acta Crystallogr 32A:751–767

Simon S, Kuehner S, Davis A, Grossman L, Johnson M, Burnett D (1994) Experimental studies of trace element partitioning in Ca, Al-rich compositions: anorthite and perowskite. Geochim Cosmochim Acta 58(5):1507–1523

Sinton J, Bergmanis E, Batiza R, Rubin K, Gregg T, Grønvold K, White S, Macdonald K, Van Dover C, Cormier M, Ryan W, Aigner-Torres M, Popels L, Boyle E, Shah A, Jin W (1999) Volcanological investigations at superfast spreading: results from R/V Atlantis cruise 3–31. Ridge Events 10(1):17–23

Smith J, Brown W (1988) Feldspar minerals, 2nd edn, vol 1, Springer, Heidelberg

Sun C, Williams RJ, Sun SS (1974) Distribution coefficients of Eu and Sr for plagioclase-liquid and clinopyroxene-liquid in oceanic ridge basalt: an experimental study. Geochim Cosmochim Acta 38:1415–1433

Thy P, Lesher CE, Mayfield JD (1999) Low-pressure melting studies and basalt and basaltic andesite fro the southeast Greenland continetal margin and the origin of dacites at site 917. In: H.C. L, Duncan AR, Allan JF, Brooks L et al (eds) Proceedings of the ocean drilling program, scientific results, vol 163. Ocean drilling program, College Station, TX, pp 95–112

Tormey D, Grove T, Bryan W (1987a) Experimental petrology of normal MORB near the Kane Fracture Zone: 22°–25°N, mid-Atlantic ridge. Contrib Miner Petrol 1987:121–139

Tormey DR, Grove TL, Bryan WB (1987b) Experimental petrology of normal MORB near the Kane fracture zone: 22–25°N, mid-Atlantic ridge. Contrib Miner Petrol 96:121–139

Urusov V, Dudnikova V (1998) The trace-component trapping effect: experimental evidence, theoretical interpretation, and geochemical applications. Geochim Cosmochim Acta 62:1233–1240

Weill DF, McKay GA (1975) The partitioning of Mg, Fe, Sr, Ce, Sm, Eu and Yb in lunar igneous systems and a possible origin of KREEP by equilibrium partial melting. In: Proceedings of Lunar science conference 6th, 1143–1158

Wenk HR, Wilde WR (1973) Chemical anomalies of lunar plagioclase, described by substitution vectors and their relation to optical and structural properties. Contrib Mineral Petrol 41(2):89–104

Wenk HR, Wilde WR, Mueller WF (1973) Lunar plagioclase: a study of feldspar chemistry and its relation to optical and structural properties. In Lunar Science IV, Lunar Science, Institute of Houston, Texas, Abstracts, pp 781–783

Wilke M, Behrens H (1999) The dependence of the partitioning of iron and europium between plagioclase and hydrous tonalitic melt on oxygen fugacity. Contrib Mineral Petrol 137:102–114

Yang H-J, Kinzler RJ, Grove TL (1996) Experiments and models of anhydrous basaltic olivine-plagioclase-augite saturated melts from 0.001 to 10 kbar. Contrib Mineral Petrol, p 124

Zeng R (1985) $CaMgSi_3O_8$, the MacKenzie's molecule, a possible indicator of supercooling. Bull Volcanol 108:713–718